



## Overview of automotive structural composites technology developments in Japan



Takashi Ishikawa <sup>a,\*</sup>, Kazuaki Amaoka <sup>a</sup>, Yuichi Masubuchi <sup>b</sup>, Tetsuya Yamamoto <sup>b</sup>, Atsuhiko Yamanaka <sup>c</sup>, Masahiro Arai <sup>c</sup>, Jun Takahashi <sup>d</sup>

<sup>a</sup> National Composites Center Japan (NCC), Nagoya University, Furoh-cho, Chigusa-ku, Nagaoya-shi, Japan

<sup>b</sup> Department of Materials Physics, School of Engineering, Nagoya University, Furoh-cho, Chigusa-ku, Nagaoya-shi, Japan

<sup>c</sup> Department of Aerospace Engineering, School of Engineering, Nagoya University, Furoh-cho, Chigusa-ku, Nagaoya-shi, Japan

<sup>d</sup> Department of Systems Innovation, School of Engineering, The University of Tokyo, 7-3-1, Hongo, Bunkyo-ku, Tokyo, Japan

### ARTICLE INFO

#### Article history:

Received 5 July 2017

Received in revised form

13 July 2017

Accepted 12 September 2017

Available online 18 September 2017

### ABSTRACT

The recent status of Japan's government-driven project to establish carbon fiber reinforced thermoplastic composites (CFRTP) technology for automotive applications conducted in the National Composites Center (NCC) Japan is introduced first. The baseline technology is discontinuous carbon fiber reinforced thermoplastic composites (C-LFT-D: carbon – long fiber thermoplastic-direct) using press compaction. All the components of the target car chassis made of aluminum alloy are replaced by C-LFT-D components and a 10% weight reduction with the same rigidity has been verified. The basic physics of the fiber length distribution mechanism and the experimental procedures to measure fiber length distributions are proposed. A basic theory to predict the flow behavior of extruded raw material of the mixture of melted resin and thermoplastics is proposed, and sophisticated CAE software to predict the flow patterns of the raw material is established. Measured elastic moduli of processed LFT-D plates show strong dependency on local fiber orientations and strong correlations between bending strengths and bending modulus are found. Hence, prediction of fiber orientation in the press compaction is a key point of the design of LFT-D components. The viscoelastic properties of C-LFT-D materials are characterized by using established theories. Certain important parameters, such as the shift factors, are identified by theory and experiments. The basic concepts of joining technology are also established, where ultrasonic fusion bonding is selected as the primary method. Joining procedures are defined and mechanical properties of the joints are evaluated. The essence of the other project conducted in the University of Tokyo for CFRTP applications to automobiles is also introduced. Several new composites are developed and evaluation technologies are developed.

© 2017 The Authors. Published by Elsevier Ltd. This is an open access article under the CC BY-NC-ND license (<http://creativecommons.org/licenses/by-nc-nd/4.0/>).

### Contents

1. Introduction .....	222
2. Discontinuous carbon fiber – thermoplastic composites (C-LFT-D) technology development project pursued in NCC Japan: general .....	223
2.1. Project outline .....	223
2.2. Current status of the processed components .....	225
3. Carbon fiber LFT-D: new fiber length distribution function and length measurement technique .....	225
3.1. Proposal of new fiber length distribution function .....	225
3.2. Fiber length distribution measurement technique .....	227
4. Carbon fiber LFT-D: flow prediction by basic theory and CAE .....	228
4.1. Prediction by basic theory .....	228
4.2. Prediction by CAE .....	229

\* Corresponding author.

E-mail address: [ishikawa@nuae.nagoya-u.ac.jp](mailto:ishikawa@nuae.nagoya-u.ac.jp) (T. Ishikawa).

5.	Carbon fiber LFT-D: mechanical properties of the products .....	231
5.1.	Determination of fiber orientation .....	231
5.2.	Elastic modulus properties .....	231
5.3.	Strength properties .....	233
6.	Carbon fiber LFT-D: viscoelastic properties of the products .....	233
6.1.	Introduction .....	233
6.2.	Basic theory of thermo-viscoelasticity [34,35] .....	234
6.3.	Estimation of relaxation modulus [36,37] .....	234
6.3.1.	Measurement of creep function of the LFT-D specimens .....	234
6.3.2.	Voigt model for approximation of creep function .....	234
6.4.	Relaxation modulus .....	235
6.5.	Shift factor [38,39] .....	237
7.	Carbon fiber LFT-D: ultrasonic fusion bonding technique .....	237
7.1.	Background and outline of ultrasonic fusion bonding method .....	237
7.2.	Evaluation of the mechanical properties of ultrasonic fusion bonded plates .....	238
8.	Outline of automotive composites technology development conducted in the University of Tokyo .....	240
8.1.	Continuous and discontinuous thermoplastic intermediate materials and closed-loop recycling .....	240
8.2.	Structural optimization for further weight lightening .....	242
8.3.	Functional design .....	243
8.4.	Molding and nondestructive inspection .....	243
9.	Conclusions and future prospects .....	243
	Acknowledgements .....	244
	References .....	244

## 1. Introduction

Carbon fiber reinforced plastics (CFRP) have been applied to a wide range of engineering fields in recent decades and have become indispensable technical components of modern industries. As is well known, CFRP are now identified as standard constituent materials in new aircraft structures. The coming potential application target might be automotive structures, where the use of CFRP applications is expected rapidly increase in the next two decades. A strong incentive to apply CFRP to automotive structures comes essentially from regulations aimed at reducing the CO<sub>2</sub> emission per unit distance. Fig. 1 [1] shows a worldwide list of considered regulations to reduce CO<sub>2</sub> emission per km. Among

them, the so-called EURO 6 regulation from 2020, in which a high tax will be applied to vehicles exceeding 95 g/km of CO<sub>2</sub> emission was adopted by the European Union. Because of this regulation, car manufacturers have been very seriously undertaking the development of new technologies for CO<sub>2</sub> emission reduction, particularly in Europe. Although the choice of power train types is principally crucial, the weight reduction of automotive structures is also very influential in reducing their CO<sub>2</sub> emissions. Fig. 2 [1] based on measured data by Japan's Ministry of Transport describes relationships between vehicle weight and CO<sub>2</sub> emission amount per km for many types of automobiles worldwide. This statistical chart tells us that 100 kg weight saving in each automotive leads to a reduction in CO<sub>2</sub> emission of 20 g/km, and that just a few types of

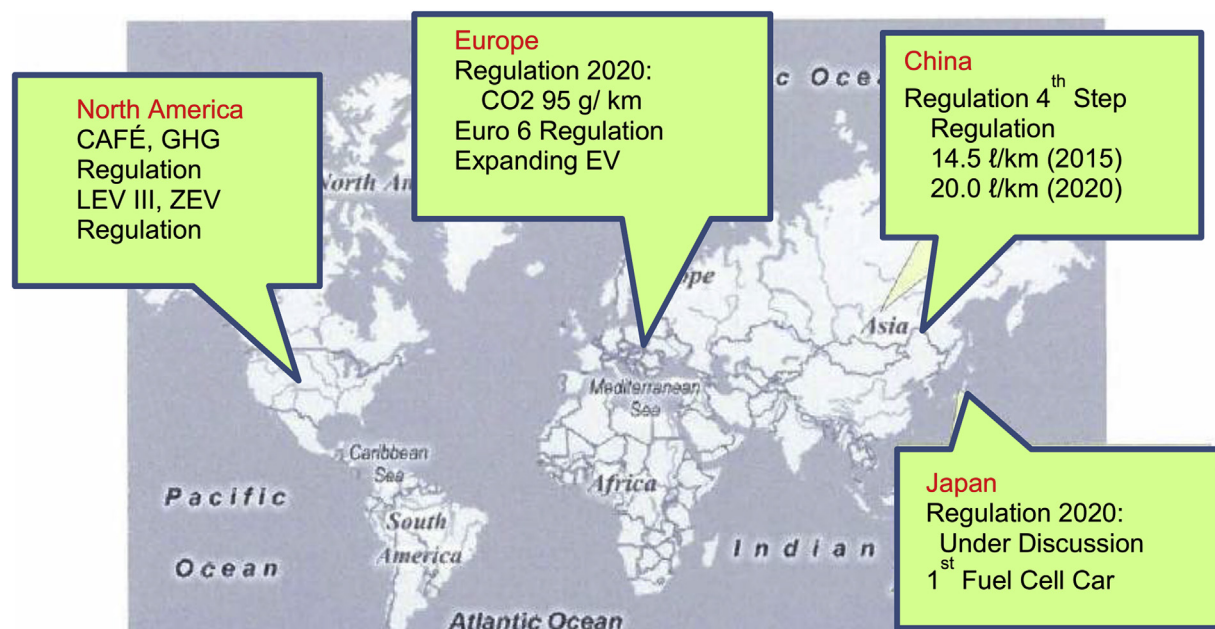


Fig. 1. Trends in global regulations applied to cars for environmental awareness: Critical CO<sub>2</sub> emission or gas mileage.

existing automobiles satisfy the future Euro 6 regulations. Thus, the effort to pursue lighter-weight cars has recently become a serious challenge for worldwide car manufacturers.

There are several alternatives to reduce car weight: employment of lighter materials, increase of functionality of components and innovations in the car system design, and so on. The employment of new lightweight material such as high-tensile steel, aluminum alloy, and composites is the most direct and effective means of weight reduction. Among those means, applications of CFRP to mass production automotive bodies have been widely adopted, particularly in German cars, such as BMW and Audi. Their technology is mainly based on so-called high-pressure resin transfer molding (HP-RTM) using carbon fiber textiles and fast-curing epoxy resins. However, there are several drawbacks in this technology, including difficulties in much higher rate of production, carbon textile wastes intrinsic to cutting, and the slow adhesion process currently required to join surrounding components.

CFRP based on thermoplastic matrix (CFRTP), particularly discontinuous carbon fiber reinforced thermoplastic composites, could be one option to solve some of the abovementioned drawbacks. The world's first fuel cell car "Toyota Mirai" adopted CFRTP [2] using a thermoplastic matrix resin reinforced by a two-dimensional paper-like carbon fiber mat for its fuel cell stack tray. The production rate of this composite component is not as high as the rate of true mass production car components of 100,000 units per year. Hence, CFRTP components utilizing more productive process technologies are strongly requested by global automotive industries. One possible solution might be the technology known as "Long Fiber Thermoplastic – Direct (Consolidation)", abbreviated as LFT-D, originally developed in Fraunhofer Institute in Germany using glass fiber. However, even in Germany, LFT-D technology using carbon fiber is still under development [3], as far as the authors know. In the National Composites Center (NCC) Japan established in Nagoya University, the development of this carbon fiber based LFT-D technology (C-LFT-D) development has been researched in the past five years and some remarkable automotive chassis components were successfully produced recently. In parallel to this activity, an alternative technology of discontinuous

carbon fiber reinforced thermoplastic composites has been developed at the University of Tokyo by professor Takahashi's group. Their typical products are randomly oriented ribbon-like pieces, which are consolidated composites based on ultrathin thermoplastic UD prepreg, so-called UT-CTT [4]. They are also trying to fabricate automotive component models using this kind of raw material. In this review article, the current development status and some basic scientific outputs related to C-LFT-D technology and Tokyo University's technology will be introduced. Owing to the sensitivity of the technology, some real data of the properties cannot be disclosed in certain chapters; instead, normalized relative data will be used for descriptions. The authors apologize for this situation and request the understanding of the readers.

## 2. Discontinuous carbon fiber – thermoplastic composites (C-LFT-D) technology development project pursued in NCC Japan: general

### 2.1. Project outline

Based on the strong requests from Japan's automotive industries and carbon fiber manufacturers, the Ministry of Economics and Trade and Industries (METI) of Japan's Government decided to start a technology development project from Fiscal Year 2013 for CFRP applications to automotive structures. One fortunate situation prior to this project starting was the foundation of the National Composites Center (NCC) Japan in Nagoya University, where basic facilities for production of C-LFT-D components were already installed, such as a large high-speed hydraulic press of 3500 ton weight capacity, indicated in Fig. 3. This project is a government–industry program and industrial interests invest some of the project costs. The main purpose of this project is to establish CFRTP composites technology for automotive applications, with a particular focus on C-LFT-D, as stated previously. The project goal is to replace all the components of a current aluminum alloy chassis by C-LFT-D components with slightly lighter weight (10%) and the same rigidity of the baseline aluminum chassis, and to verify the superiority of C-LFT-D structures in terms of rigidity and lighter

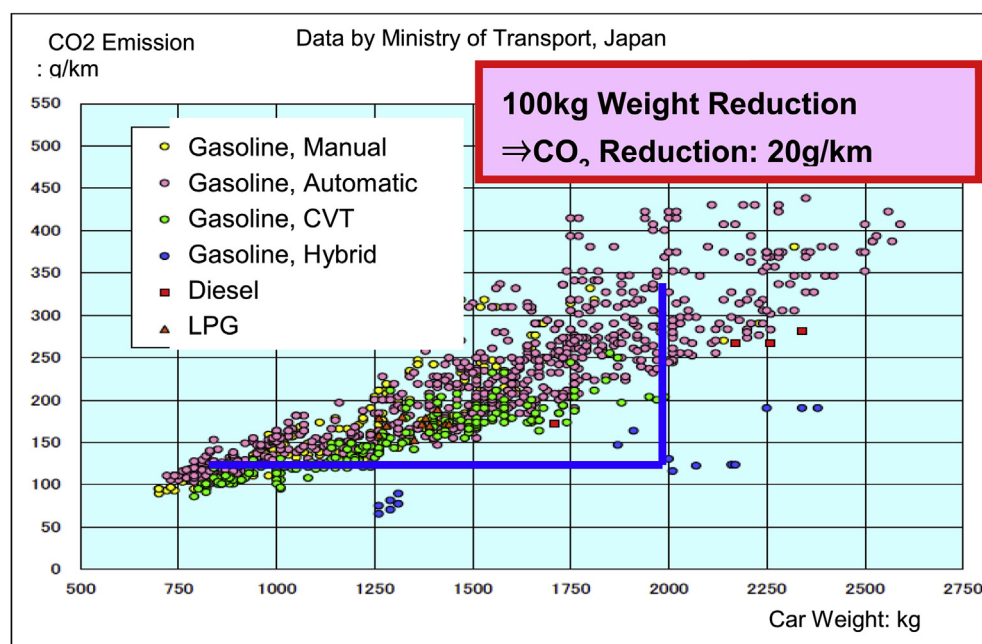


Fig. 2. Relationships between car weight and CO<sub>2</sub> emission per unit distance (g/km) based on the data obtained by Ministry of Transportation, Japan's Government.



Fig. 3. Large high-speed hydraulic press of 3500 ton weight capacity installed in national composites center Japan in 2013: Key facility for LFT-d technology.

weight. As the baseline car, a “Lotus Elise” was selected because the full chassis of this car was already made of aluminum alloy. 1 min was determined as the target production tact time of C-LFT-D components. In order to explain the overall technology roadmap of CFRP in terms of mechanical properties and production rates, Fig. 4 will be indicated here. The vertical axis is a conceptual scale of mechanical properties and the horizontal axis is a conceptual scale of productivity, which is a synonym of production tact time. A shorter time is considered to be superior and the right direction is better. A good balance between higher mechanical properties of C-LFT-D and shorter tact time is a technological goal on the material side scope of the current project. For easier overall understanding,

the concept of a large-scale LFT-D processing line system is indicated in Fig. 5. From here on, C-LFT-D will be referred to simply as LFT-D. Thermoplastic pellets, PA6, which have been adopted so far in this project, are supplied to the first axis of the extruder and melted resin is fed to screws of the second axis, and continuous carbon fiber bundles from their bobbins are supplied to a certain portion of the screw. The carbon fibers are cut or broken into short fibers and blended with the melted resin, and extruded from a sophisticatedly designed nozzle. If the temperature of the extruded raw material is sufficiently higher than the melting temperature of the matrix resin, it looks soft and contains a large volume of air. Therefore, the extruded material is called a “Futon” in NCC Japan, which originally refers to a cotton mat of a Japanese foldable bed. Because the temperature of the “Futon” rapidly goes down after extrusion, a temperature control chamber was placed in front of the large press. Additionally, a material handling system composed of a fast moving robot and a specially developed end effector with a heat keeping system was developed and used for short time supply of the raw extruded material to the press. When the compaction is performed by the press, air in the “Futon” must be excavated by valve operations into a large vacuum chamber, which is an important component of the system. The compaction speed of the press is a very important parameter consisting of a process parameters window of LFT-D and a highly confidential point in the process expertise. Although in the initial term of the first project year, 2013, it was very difficult to fabricate even a flat plate of the size of 1400 × 800 mm, the processing know-how has gradually improved and a complete (fully filled into the mold: full shot) plate was obtained. The next target was the trial processing of a stiffened element as a model of a side sill, which is an important component of the target chassis, where the flow capability of the “Futon” must be checked. Fig. 6 left indicates a simple stiffener element of a five-wall box without internal structures and Fig. 6 right indicates a stiffener element with crossing internal web walls. Although the latter type of the component is very difficult to fabricate by using continuous fiber reinforcement, prepreg, or dry fabric, it could be easily obtained in the case of LFT-D by male mold machining and satisfactory flow capability of the extruded material. This

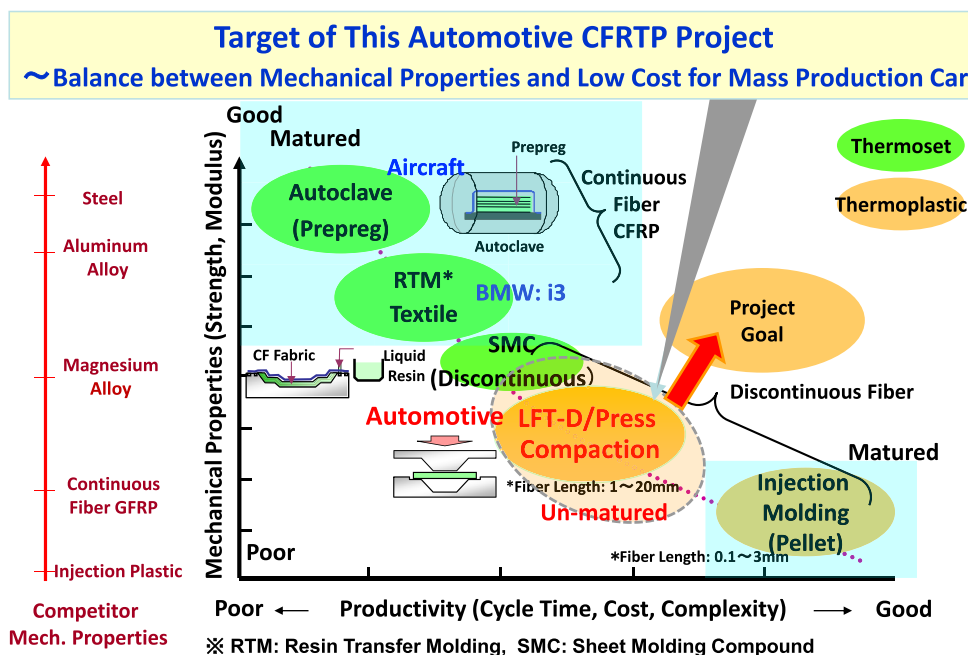


Fig. 4. Technology Road Map of CFRP in Terms of Mechanical Properties and Production Rate (Short Tact Time is Superior).

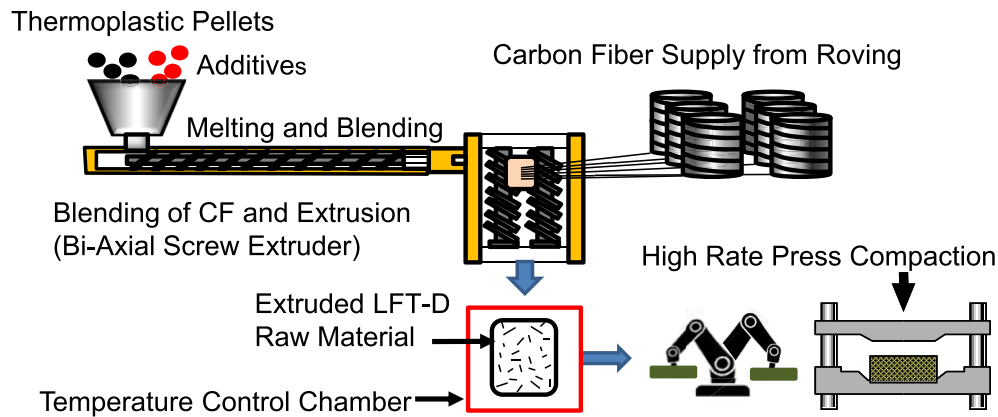


Fig. 5. Concept of large-scale C-LFT-d processing system using biaxial extruder, temperature control chamber, material handling robot and high-speed press.

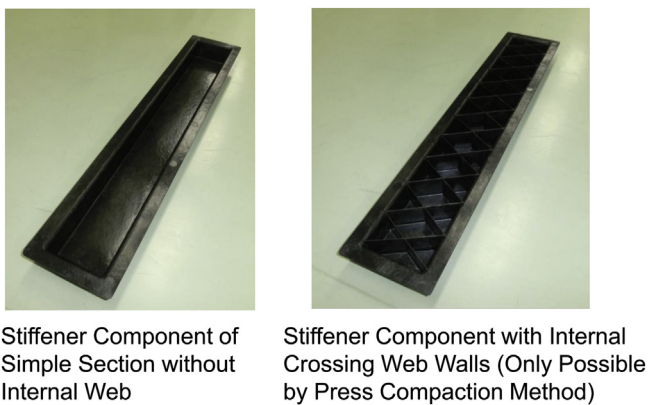


Fig. 6. Examples of fabricated model stiffener elements: Without and with internal web wall structures, implication of design directions of LFT-d structures.

experiment implied a design direction of LFT-D structure whereby the rigidity requirement of components will be compensated by their structural design, even though the material elastic modulus of LFT-D is inferior to that of continuous fiber composites. However, it was also understood that a hybridization of LFT-D with continuous fiber CFRTP of the same matrix must be developed for higher rigidity components. This kind of hybrid processing was found not to be difficult if a proper pre-heating of CFRTP prepreg of the same matrix as LFT-D was performed. Based on these findings, the steps of the project became rather smooth from the second year, 2014. The project technical items to be pursued and the whole timetable of the five-year project are indicated in Fig. 7 where FY 2017 is the last term of the 1st phase of this project. The continuation to the 2nd phase is under discussion.

## 2.2. Current status of the processed components

Following the schedule indicated in Fig. 7, several kinds of chassis components were fabricated in NCC Japan. Because a floor panel of 2 m<sup>2</sup>, the largest component of the chassis, is the most difficult to fabricate, the first project target was this component. By establishing a very narrow process window, a high quality product of this floor panel was obtained in the summer of 2015. The next target was a side sill inner, where a hybrid processing using fabric (twill) prepreg with the same PA6 matrix as LFT-D was required in order to fulfill the necessary stiffness conditions. Photos of these two components are shown in Fig. 8. A practical optimal design process was introduced to minimize the structural weight of the

whole chassis. The computed optimization results describe serious variation in thickness corresponding to side sill locations. If we employ continuous reinforcement technologies, such as prepreg or dry fabrics and RTM, it is very difficult and costly to fabricate such variable thickness components. However, for LFT-D processing technology, it is very easy to fabricate such a component, as already explained regarding stiffener elements, indicated in Fig. 6. It can be accomplished only by providing curved surface shapes of molds to realize the computed optimal thickness distribution. This point is a great advantage of LFT-D processing technology. During the first phase of the project (2013–2015), the process prediction capability of the computer-aided engineering (CAE) software was very much improved, to include several important factors, such as pressure, time to raw material flow arrival, local fiber orientation, and local elastic modulus, among others. This capability improvement has contributed significantly to reducing the number of trial-and-error cycles in LFT-D processing. Full-quality subsidiary components have been fabricated during FY 2016 at least once and improvements of the process details were undertaken at the beginning of FY 2017. The assembly of the whole chassis made by LFT-D with continuous fiber textile prepreg as a stiffening device in the inner side sills will be completed in the spring of 2017. The assembled chassis will be subjected to several structural tests for evaluation of the degree of fulfillment of the project targets.

## 3. Carbon fiber LFT-D: new fiber length distribution function and length measurement technique

### 3.1. Proposal of new fiber length distribution function

Owing to its significant influence on the material properties, the fiber length distribution is of great interest for fiber composites [5,6]. In particular, for thermoplastic polymers changes in fiber length distribution are unavoidable during material processing [7–10]. In this respect, a method of analysis of fiber length distribution is necessary to clarify the effects of processing conditions.

The fiber length distribution has been discussed in terms of Weibull distribution (also called as Tung's distribution) [11,12], in which the probability is written as

$$P(l; \lambda, k) = \frac{k}{\lambda} \left(\frac{l}{\lambda}\right)^{k-1} \exp\left\{-\left(\frac{l}{\lambda}\right)^k\right\} \quad (3.1)$$

Here,  $k$  is the Weibull modulus and  $\lambda$  is the scale parameter. Equation (3.1) has been reported for its capability to fit experimental data [13,14]. However, we have found that the parameters  $k$

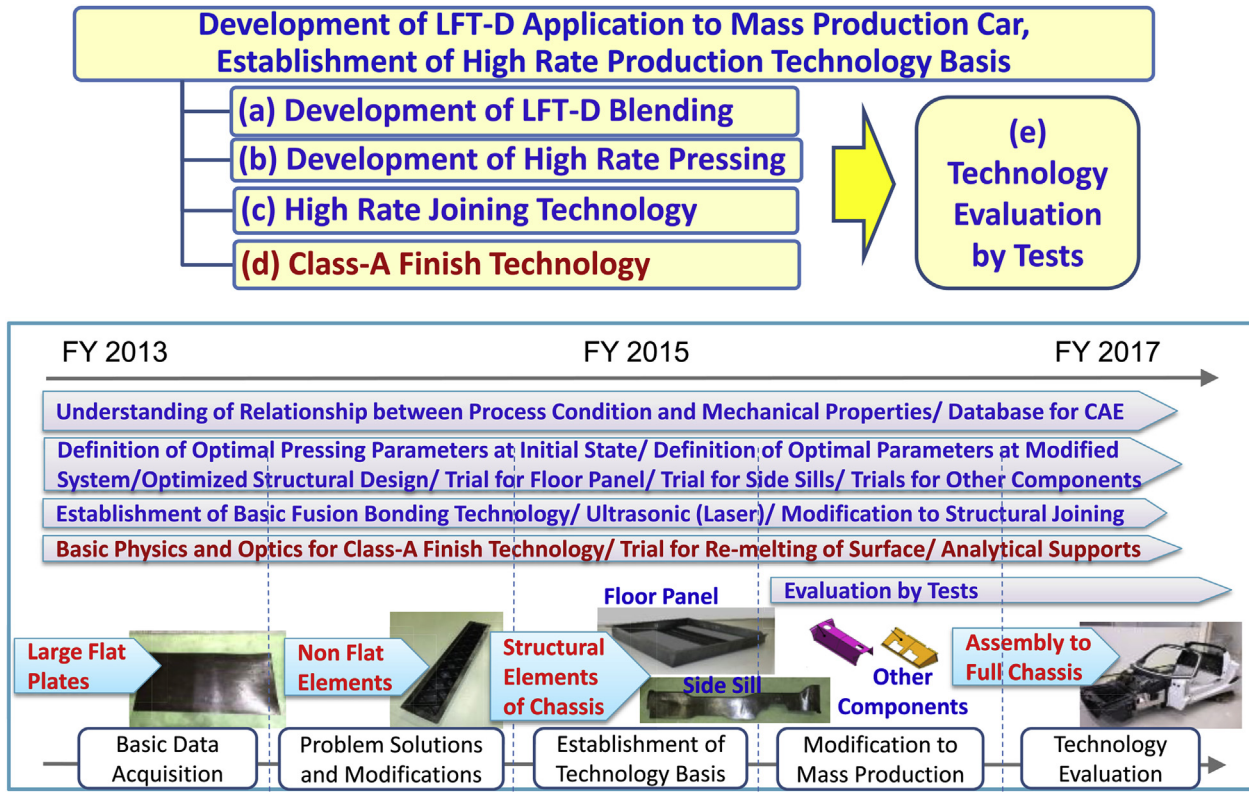


Fig. 7. Technological Items to be Pursued and Five-Year Project Schedule.

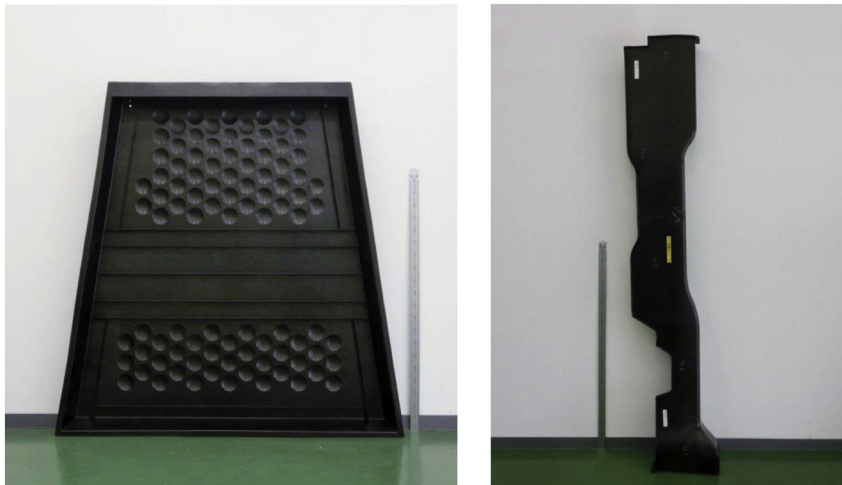


Fig. 8. Photos of Typical Chassis Components fabricated by LFT-D Technology. Left: Floor Panel of 2 m<sup>2</sup> area; Right: Side Sill Inner of 2 m in length.

and  $\lambda$  are not always in good correlation with the material properties (as discussed later). In addition, the stochastic process behind the Weibull distribution [15] may differ from what is attained during the present process.

As a possible additional option for the functional form of fiber length distributions, we have proposed the equation below [16].

$$P(l; \lambda_a, \lambda_b) = \frac{1}{\lambda_a - \lambda_b} \left[ \exp\left(-\frac{l}{\lambda_a}\right) - \exp\left(-\frac{l}{\lambda_b}\right) \right] \quad (3.2)$$

Here,  $\lambda_a$  and  $\lambda_b$  are the parameters for two different Poisson

processes involved in the assumed stochastic process for Equation (3.2). The first term on the right hand side of Equation (3.2) corresponds to an ordinal Poisson process in which the fiber is subjected to random scissions with the probability of scission per unit length of  $1/\lambda_a$ . In our observations, for the long fibers the distribution can be reasonably described by exponential decay functions (at least in some cases, as shown later), and the first term in Equation (3.2) is used to describe such behavior. However, the Poisson process assumes that the highest probability is assigned to a fiber length of zero. Although in some works from the literature, such a distribution is reported wherein the length distribution for

short fibers is not separated, most recent studies have revealed that the distribution has a peak before the exponential tail (see Ref. [13] for example). Actually, the distribution around the peak is well-described by the Weibull distribution. Nevertheless, the second term in the RHS attains the peak by introducing the other Poisson process, which is inserted into the successive scissions owing to the first Poisson process. The second Poisson process describes a random block of successive scissions with the average block length of  $\lambda_b$ . In other words, the block becomes ineffective with the probability per unit length of  $1/\lambda_b$ . We expect that the first Poisson process (for the scission) will be affected by the processing conditions, such as the magnitude of extrusion, whereas the second Poisson process (for the block) is dominated by the mechanical properties of fiber. The distribution function shown in Equation (3.2) has been applied to describe the topological structure of polymer melts [17].

Fig. 9 shows a comparison of Equations (3.1) and (3.2) to an experimental dataset for LFT-D products reported in the literature [3], in which a carbon fiber with a diameter of 7.2  $\mu\text{m}$  is compounded with nylon-6 and the fiber volume fraction is 35%. In the linear plot (top panel), the Weibull distribution seems in better agreement with the data, specifically around the peak. On the other hand, in the semi-logarithmic plot (lower panel), the proposed distribution attains a better fitting in the long tail region that dominates the mechanical properties of the product.

Fig. 10 shows the correlation between the parameters in the distribution functions and the tensile strength for the glass fiber composites, for which the extrusion conditions were varied to modify the fiber length. The experimental data was taken from the literature [18], in which the base resin is nylon-6 and the glass fiber diameter is 13  $\mu\text{m}$ . Among the length parameters, i.e.,  $\lambda$  in Equation

(7.1) and  $\lambda_a$  and  $\lambda_b$  in Equation (3.2),  $\lambda_a$  has a remarkable correlation with the tensile strength. We have similar results for the elastic modulus and impact strength. These results suggest that the Poisson process for scission considered in Equation (3.2) reasonably describes the extrusion process.

### 3.2. Fiber length distribution measurement technique

It is important for development of composites reinforced with discontinuous fibers to evaluate their fiber length distribution. Generally, fiber length distributions have been estimated by optical microscopic images of suspensions of fibers [19–21]. However, in this method, the relation between magnification and observation area is a strict trade-off. The numbers of fibers counted from observation area of microscopic images were less than 1000 in previous papers [19–21]. However, Lunt and Shortall pointed out that characterizing the whole distribution of the fiber in the composite made by extrusion method necessitates approximately 2000 counts [22]. Thus, the expansion of the observation area was important for measurements of fiber length in composite materials.

On the other hand, image scanning could be a solution for this requirement, because of their high-pixel images. The available image size of general scanners is greater than 100 Mpixels, meaning that a 2400 dpi scan image allows the coverage of more than 100 mm  $\times$  100 mm. Recently, fiber length analyzers with a high-resolution scanner and software have already been made into products [23]. However, the characteristics of scanned images have not been reported.

We have investigated the characterization of the measurement method for carbon fiber length in a large observation area using a general commercial scanner [24]. Fig. 11 shows a scan image of a polyvinyl alcohol (PVA) sheet in which discontinuous carbon fibers were dispersed. The PVA sheet shown in Fig. 11 was prepared by casting from a suspension of carbon fibers and PVA aqueous solution, and was scanned by a general commercial scanner apparatus with a resolution of 2400 dpi. The observation area is 182 mm  $\times$  120 mm, which is larger than that in microscopic methods. It is also found that the fibers in the scanned image are clearly observable.

Fig. 12 shows a length distribution of carbon fibers in the PVA sheet obtained from the scanned image shown in Fig. 11. The

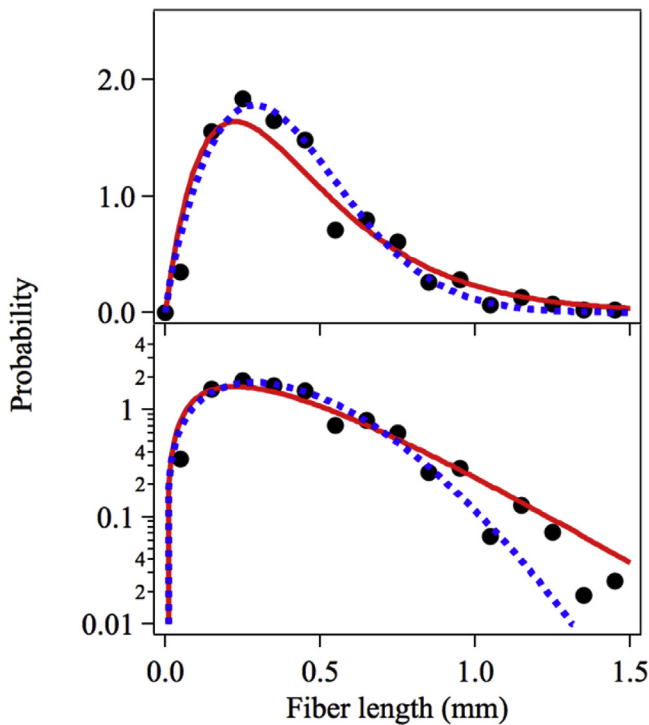


Fig. 9. Fiber length distribution for an LFT-D product consisting of nylon-6 and carbon fiber with the fiber volume content of 35% [17]. Black dot indicates the experimental data. Red solid and blue dotted lines are Equations (7.1) and (7.2) with the parameters that achieve the best fit. Top and bottom panels show the distribution in linear and semi-logarithmic plots, respectively. (For interpretation of the references to colour in this figure legend, the reader is referred to the web version of this article.)

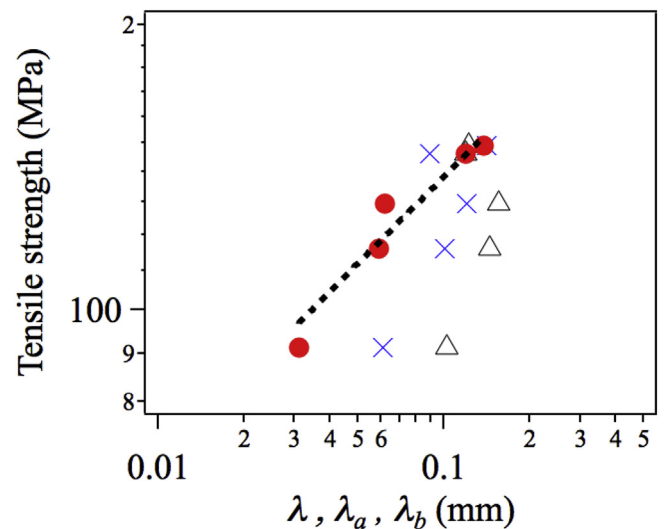
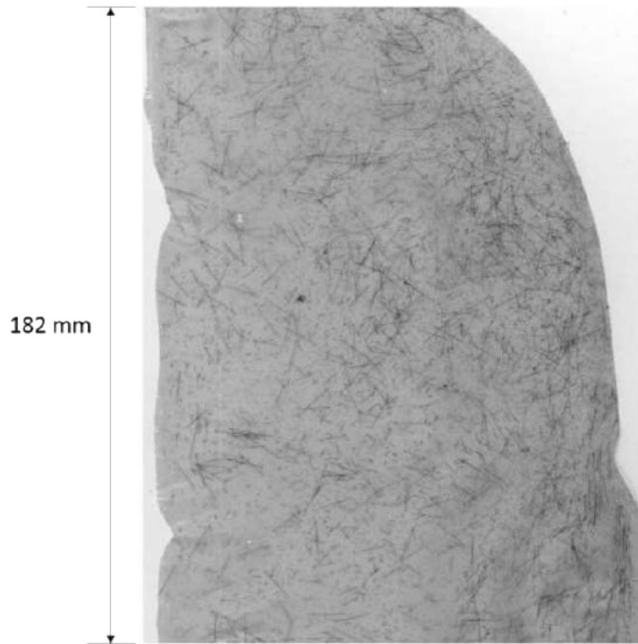


Fig. 10. Correlation between tensile strength and the length parameters for nylon-6/glass fiber composites reported in Ref. [18]. Crosses, circles and triangles show  $\lambda$  in Equation (7.1) and  $\lambda_a$  and  $\lambda_b$  in Equation (7.2), respectively.



**Fig. 11.** Scanned image of the PVA sheet in which discontinuous carbon fibers are dispersed. This image was obtained by a general commercial scanner apparatus with resolution 2400 dpi.

number of fibers counted from this image is more than 25000. Therefore, it is possible to expand the observation area and to measure the length of more than 25000 discontinuous carbon fibers using a general commercial scanner.

We have compared the fiber lengths measured from scanned image to those from optical microscope for the five selected fibers and it was also found that fiber lengths measured from scan image are different from those estimated by an optical microscope, as shown in Table 1 [24]. The fiber length measured from the scan image is defined as  $L_{sc}$ , and that measured from optical microscope is defined as  $L_{mi}$ . The mean values of  $L_{sc}$  ( $L_{sc}$ ) were estimated from 10 scanned images of the same fiber. The measurement error

decreases by increasing fiber length.

Fig. 13 shows the relationship between the coefficients of variation of  $L_{sc}$  (CV) and the inverse of  $L_{sc}$ . CV is proportional to the inverse of  $L_{sc}$ , which means that the measurement accuracy decreases as the carbon fiber length decreases. These results suggest that measurement lower limit of fiber length from a scanned image is estimated by the relationship.

#### 4. Carbon fiber LFT-D: flow prediction by basic theory and CAE

##### 4.1. Prediction by basic theory

In the LFT-D process, automobile parts are produced by high-speed compression molding. The temperature of the molds is set lower than the solidification temperature of constituent thermoplastics (defined by the temperature at which the mixture stops flowing) and mixtures of polymer melt and carbon fibers locally stop flowing from the interface between the mixture and the molds. Owing to the fact that carbon fibers have a relatively large thermal conductivity, the processability of carbon fiber-thermoplastic composites may be limited by the solidification process. Simulations for analogous situations have been performed to find the optimal condition for practical situations [25–27]. However, a simple theoretical model may be useful to capture the physics involved in the molding process of LFT-D and to analyze the experimental results.

Here, we treat cases in which a cylindrical sample (radius  $a_0$  and height  $h_0$ ) of a mixture of polymer melt and carbon fibers is

**Table 1**

Mean value of the measurements ( $L_{sc}$ ), their sample standard deviation and their errors.

$L_{mi}$ (mm)	$L_{sc}$ (mm)	$\frac{L_{sc}-L_{mi}}{L_{mi}}$
1.334	1.357	0.017
0.595	0.591	-0.006
0.226	0.231	0.021
0.099	0.082	-0.172
0.067	0.060	-0.102

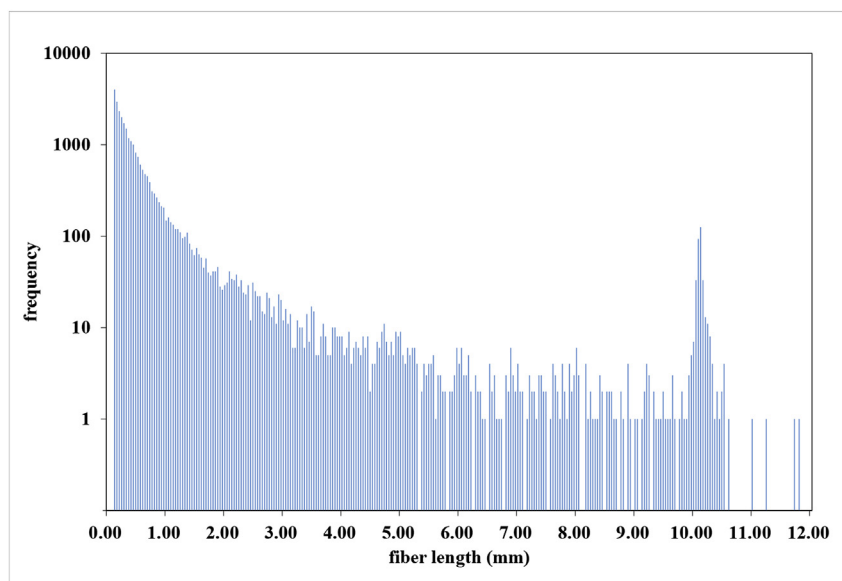


**Fig. 12.** Fiber length distribution counted from scanned image, shown in Fig. 11.

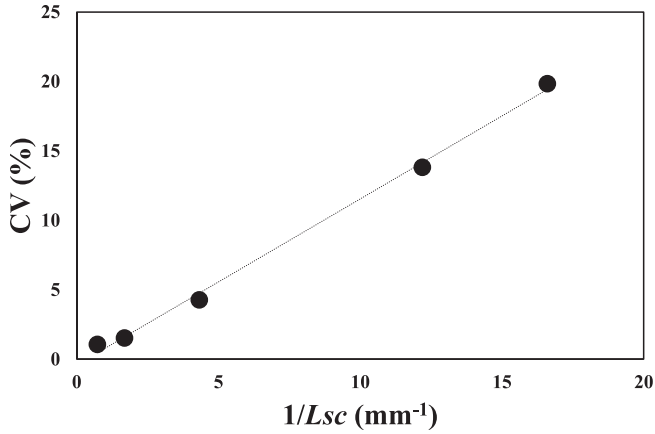


Fig. 13. Relationship between the coefficient of variation of  $L_{sc}$  and the inverse of  $L_{sc}$ .

compressed by parallel plates with a constant speed  $V_0$ . For simplicity, we treat the mixture as an incompressible Newtonian fluid of viscosity  $\eta_s$  and neglect the anisotropy with respect to the viscosity and thermal conductivity (although such mixtures, in general, show anisotropy due to the orientational ordering of carbon fibers). The mixture locally stops flowing when the local temperature is lowered to the solidification temperature  $T_{sol}$ ; the material shows solidified regions near the surface of the molds. We apply the non-slipping boundary condition at the interface between the solidified region and fluid region. The compression is terminated at time  $\tau_c$ , when the entire thickness is solidified.

This model predicts that the compression time  $\tau_c$  is determined by a single parameter  $\chi$  and has the form

$$\frac{\tau_c}{\tau_m} = \frac{1}{1 + \chi}. \tag{4.1}$$

The parameter  $\chi$  has the form

$$\chi = \alpha^2(\tilde{T}_s) \frac{D_h}{h_0 V_0}, \tag{4.2}$$

where  $\alpha^2(\tilde{T}_s)$  is the temperature factor and  $D_h$  is the thermal diffusion constant of the mixture.  $\tilde{T}_s (= (T_s - T_{mld}) / (T_0 - T_{mld}))$  is the rescaled temperature ( $T_{mld}$  is the temperature of the molds and  $T_0$  is the temperature of the mixture at  $t = 0$ ). The temperature factor  $\alpha^2(\tilde{T}_s)$  has an asymptotic form  $-\pi^2 / \log(\pi \tilde{T}_s / 4)$  for  $\tilde{T}_s < 1$  (the gray broken curve in Fig. 14) and  $-16 \log(\sqrt{\pi}(1 - \tilde{T}_s))$  for  $\tilde{T}_s \sim 1$  (the gray dotted curve in Fig. 14). The parameter  $\chi$  is indeed the ratio of the time  $\tau_m (= h_0 / V_0)$ , in which the molds are closed for  $\alpha^2(\tilde{T}_s) \rightarrow 0$ , and the time  $\tau_s$ , in which the entire material is solidified for  $V_0 \rightarrow 0$ . The parameter  $\chi$  is independent of the viscosity  $\eta_s$  because the flow dynamics of the mixture are solely determined by the fact that the mixture is incompressible as long as it is compressed with a constant speed; this theory is also effective for materials that follow non-Newtonian constitutive relationships. The thickness of the product has the form  $h_0 \chi / (1 + \chi)$  and thus decreases upon decreasing the parameter  $\chi$ . The parameter  $\chi$  is thus an important parameter that determines the processability of thermoplastic composites.

The carbon fibers in a mixture show reorientation due to the applied shear and elongational deformation during a compression. The orientational order of these fibers is characterized by a tensor order parameter that has a dyadic form

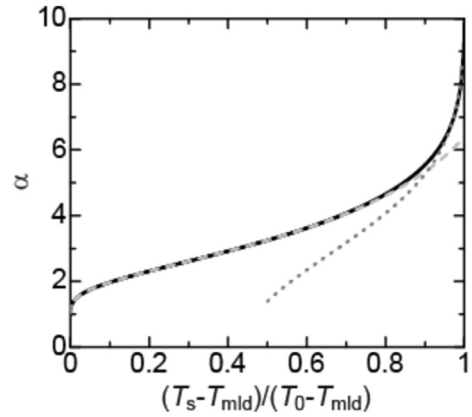


Fig. 14. The temperature factor  $\alpha^2(\tilde{T}_s)$  in eq. (4.2) vs the rescaled temperature  $\tilde{T}_s (= (T_s - T_{mld}) / (T_0 - T_{mld}))$  (the black solid curve). The asymptotic forms of this factor are shown by the gray broken and dotted curves (see also the discussion below Equation (4.2)).

$$\mathbf{Q}(\mathbf{r}, t) = \mathbf{u}\mathbf{u} - \frac{1}{3}\mathbf{I}, \tag{4.3}$$

where  $\mathbf{u}$  is the unit vector that is parallel to the constituent carbon fibers and  $\langle \cdot \rangle$  is the average with respect to the orientational distribution function of the carbon fibers. This distribution function gives the probability of finding fibers that are directed towards  $\mathbf{u}$  at the position  $\mathbf{r}$  and time  $t$ . This order parameter is symmetric with respect to the reversal of the orientation of the carbon fibers,  $\mathbf{u} \rightarrow -\mathbf{u}$ , and is a parameter that is used to characterize the orientational order of nematic liquid crystals [28]. The dynamics of the tensor order parameter is treated by using the standard methods of statistical mechanics for cases in which the steric interactions between carbon fibers are negligible [29].

For cases in which a cylindrical sample is compressed by parallel plates, the polymer melt flows to the radial direction and thus the carbon fibers orient toward this direction. The extent of such an orientational ordering is represented by using  $\Delta Q = \langle \sin^2 \theta \cos^2 \phi \rangle$ , where  $\theta$  is the polar angles of the fibers with respect to the compression direction and  $\phi$  is the azimuthal angle of the fibers with respect to the direction of the flow direction (see also the inset of Fig. 15). Our theory predicts that the local orientational order parameter  $\Delta Q$  of the product in the radial direction is a non-monotonic function of the distance from the central plane when the orientational distribution of fibers at  $t = 0$  is random and uniform (see Fig. 15). This is because the orientational dynamics of fibers near the surface are quenched before fibers show reorientation by applied shear and the front of the solidified region, at which the applied shear rate is maximum, advances towards the central plane, at which the applied shear rate is zero. We envisage a theory that predicts the dependence of the elastic modulus on the process parameters via the tensor order parameter.

Our theory does not take into account the processes before the materials are compressed or the details of the solidification processes. It would be of interest to take into account the essential features of these processes in an extension of our theory to capture the physics behind the compression molding of thermoplastic composites.

#### 4.2. Prediction by CAE

The theory explained in the previous section is a basic but highly physical one, which is very helpful to establish a strategy of press

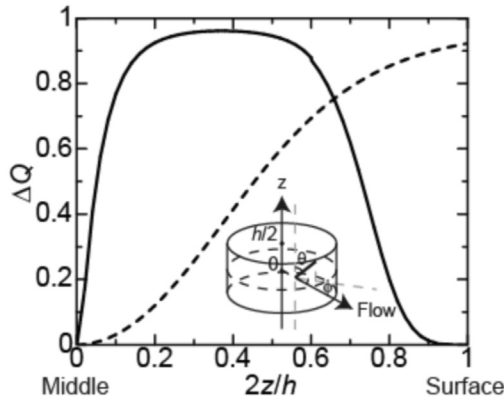


**Fig. 15.** The orientational order parameter  $\Delta Q(r)$  of carbon fibers towards the radial direction vs the distance  $z$  from the central plane, normalized by the thickness  $h$ , for cases in which the mold temperature is lower than the melting temperature of the composite (solid line) and in which the heat and cool technique is used (broken line). [We calculated for the distance  $r/a_0 = 0.5$  from the central axis, the initial aspect ratio  $a_0/h_0 = 4.0$ , the rescaled diffusion constant  $D_n/(h_0V_0) = 0.379$ , and the rescaled temperature  $\bar{T}_s = 0.5$ .]

compaction speed profile and mold temperature setting. However, as has been explained, the existence of fiber is neglected in this theory, i.e., the treated medium is not a composite but rather a viscous resin. Therefore, if the requirements of fiber orientation prediction have been increased, we need a sophisticated CAE tool for that purpose. The software developed by Toray Engineering Co. LTD named 3D TIMON could be one of the best candidates among many software groups predicting fiber orientations in injection molding process. This software utilizes a base method called “Direct Fiber Simulation (DFS)” and its theoretical details are given elsewhere [30]. Another important point in the theory is the modeling of a longer fiber as an assemblage of rods and again, the theoretical details are referred to in Refs. [30] and [31]. In the course of the present project, Toray Engineering Company has been challenging to modify and improve this software to predict fiber orientations in compression molding of LFT-D extruded material, “Futon.” By conducting many experiments to estimate viscous properties of “Futon,” its capability to predict fiber orientations during the process of compression molding by a press has been significantly improved recently. Fig. 16 indicates the predicted fiber orientations in a trial calculation of press compaction of a flat plate of 1400 by 800 mm, where approximately 403,000 elements and 849,000 fibers were utilized for a 30% fiber volume fraction plate and where a fiber corresponds to a rod. The model thickness after

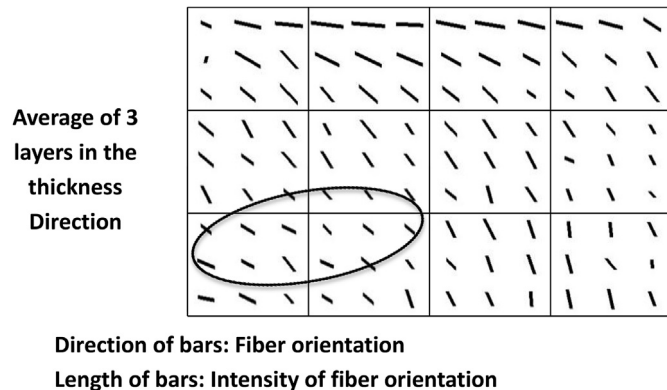


**Fig. 16.** Example of fiber orientation predictions by improved 3D TIMON developed by Toray Engineering Co. LTD for LFT-D compaction processing.

compaction is 3 mm and the thickness of an element is 0.5 mm, i.e., six elements are assumed in the thickness direction where no symmetry conditions with respect to the central surface are assumed. On the other hand, symmetry conditions are introduced with respect to the two orthogonal in-plane axes. The plots indicated in Fig. 16 are averaged values of three elements of the lower portion of the total six elements in the thickness direction. If we compare the predicted fiber orientations in Fig. 16 with measured fiber orientations by the laser spot periodic heating method explained in the next chapter and indicated in Fig. 20, the predicted fiber orientations coincide rather well with the experimental results, except for the region marked by an elliptic circle. This discrepancy might be ascribed to a slight difference in the processing details of the large mother plates for measurements.

This software can also predict filling patterns of meted media into a mold and pressure distributions around the mold during press compaction. Fig. 17 shows the predicted filling time history of “Futon” into the mold for the case of simultaneous processing of the center member and the rear panel of the target chassis. Half the portion is shown owing to the symmetry. Approximately 1,147,000 elements and 2,634,000 fibers were utilized for a 30% fiber volume fraction “Futon.” The upper plot indicates the spreading time over the whole processing period from 0.0 to 5.1 s. It can be understood that the melted “Futon” is filled into the cavity of the mold for target components, the center member (right side) and the rear panel (left side), within initial time steps. In order to indicate the details of filling time history at these initial time steps, the left-lower plot of the spreading time is prepared for the period from 0.0 to 0.6 s. The flow fronts of “Futon” are located near four entrances of the mold cavities for excess “Futon.” This kind of cavity for excess raw materials will not be required at the final established processing of LFT-D materials. However, because the current processing is in under development phase and because the quantity of “Futon” is not an arbitrary value, this sort of cavity is sometimes required. The latest flow front reaches the edge of the rear panel at approximately 0.6 s after compaction starts, as indicated by an elliptical circle in Fig. 17. The right-lower plot indicates that the “Futon” gradually spreads into cavities for excess materials after its filling into the objective component cavities. Although an indication of pressure distribution predictions is omitted here, it is very helpful to establish the details of processing expertise, such as initial placement locations of the “Futon”.

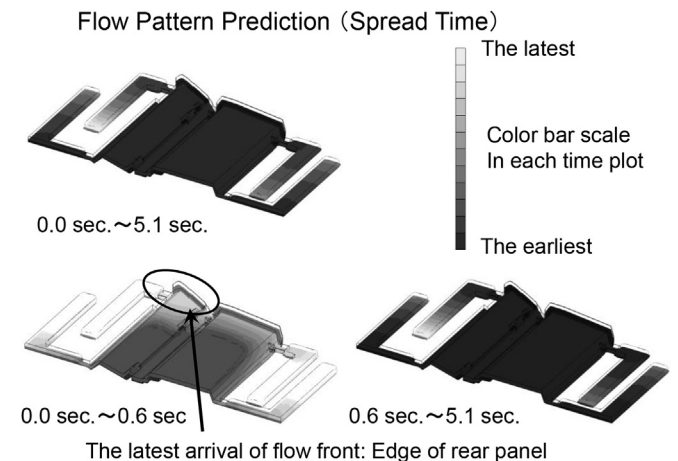


**Fig. 17.** Example of flow pattern in the filling simulation of “Futon” into mold cavities:  $V_f = 30\%$ .

**5. Carbon fiber LFT-D: mechanical properties of the products**

**5.1. Determination of fiber orientation**

After the establishment of the process window parameters, the mechanical properties of the C-LFT-D products were tending to be stabilized and became reproducible. In order to determine the mechanical properties of C-LFT-D, specimens must be prepared out of flat plates. The first technical barrier was the variety of discontinuous fiber orientations depending on the location of a specimen's mother plates of 1400 by 800 mm. This orientation variety was caused by the flow of matrix resin during press compaction. Two problems were considered to be solved related to this barrier: the first point was how to measure the fiber orientation and how to define its distribution intensity, and the second point was how to predict fiber orientation trends. Such local fiber orientation properties govern the mechanical properties, particularly the elastic modulus of this composite.

Concerning the first point, two methods were pursued in this project program, the so-called "laser spot periodic heating method" and X-ray diffraction (XRD). The first one is a completely new method based on a periodic laser spot heat source and lock-in thermography technique developed by Nagano et al. [32]. The principle is shown in Fig. 18 and the basic physics are stated below.

If periodic heating by a constant frequency ( $f$ ) laser heat source is applied to a spot on the plate as shown in Fig. 18, the periodically alternating temperature,  $T_{ac}$ , at a sensing point of distance,  $r$ , from the heating spot, can be written as follows:

$$T_{ac}(r, t) = q/4\pi Dr \exp\{i(2\pi ft - kr)\} \exp\{-kr\} \quad (5.1)$$

where  $q$  is an amount of heat,  $D$  is a thermal diffusivity, and  $k$  is a constant. The phase lag,  $\theta$ , between the heating spot and the sensing point can be written as:

$$\theta = -kr = \sqrt{\pi f/D} \quad (5.2)$$

The local thermal diffusivity,  $D_L$ , can be obtained from this equation, i.e., from the slope of the measured phase lag by lock-in thermography device, as follows:

$$D_L = \pi f / (d\theta/dr)^2 \quad (5.3)$$

The thermal diffusivity reflects anisotropy of the plate governed by local fiber orientation. In the actual fiber orientation measurement, the thermal diffusivity distribution all around the sensing point is measured and a fiber orientation density function is obtained by fitting, as shown in Fig. 19 [33]. Fig. 19 is shows typical results of the thermal diffusivity distribution (by dots) obtained for a certain C-LFT-D plate. Although the obtained fiber orientation

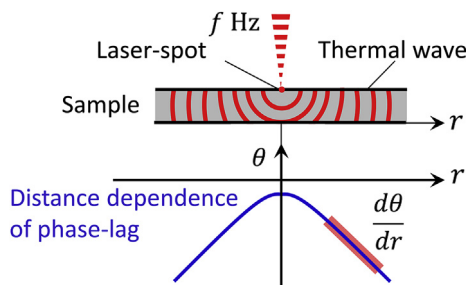


**Fig. 18.** Principle of the Thermal Diffusivity Measurement using "Laser Spot Periodic Heating Method".

density function does not necessary show an ellipsoidal shape in a polar plot, it is convenient to fit an approximate ellipse to indicate the intensity of anisotropic distribution and the major directions of the most probable fibers. Fig. 20 shows an example of the measured phase-lag distribution, which is a direct output of the lock-in thermography system and in-plane thermal diffusivity angular distribution for a large C-LFT-D plate (1400 by 800 mm). The diffusivity angular distribution is subjected to an elliptic approximation and the vector diagram is shown the lower part of Fig. 20. The location of shorter vector length indicates rather isotropy and the location of longer vector length indicates strong anisotropy. The direction of the vector indicates the direction of the fiber orientation peak direction. It can be seen that portions away from the center of the mother plate, upper left (near the wall and the free edge) and lower left (near the center line and the free edge) of the bottom plot of Fig. 20 show the most anisotropic fiber orientations. As stated earlier, the matrix resin flow during press compaction is most severe near the free edge and this flow affects the fiber orientation. It can be also understood that the fibers are oriented vertically along the vertical center line, referred to as the transverse direction (TD), whereas the horizontal direction is referred to as the machine direction (MD), corresponding to the machine extruding direction. Thus, the capability of this measurement method is well demonstrated and practical improvements in the measuring system are now undertaken.

Concerning the second method, X-ray diffraction, the details of procedure cannot be described here because a patent application about this method is undertaken. In order to solve the second problem to predict such fiber orientation behavior, sophisticated CAE software should be required. The efforts regarding this point are already stated in the later part of Chapter 4.

**5.2. Elastic modulus properties**

Based on the knowledge of position dependency of fiber orientations, the tensile and bending elastic moduli were determined for large mother plates of 1400 by 800 mm. Specimens of 25 mm in width and 140 mm in length are essentially adopted for both means of moduli measurements. In the bending moduli calculation, the nonlinear effects were not taken into account, such that the smaller bending deflection regions were selected for the calculation. As explained in the previous section, two attributes could affect the elastic modulus, the distance from the center of the plate and the direction of the specimen cutout, the MD or the TD. Fig. 21 indicates the locations and directions of the specimen cutout from the

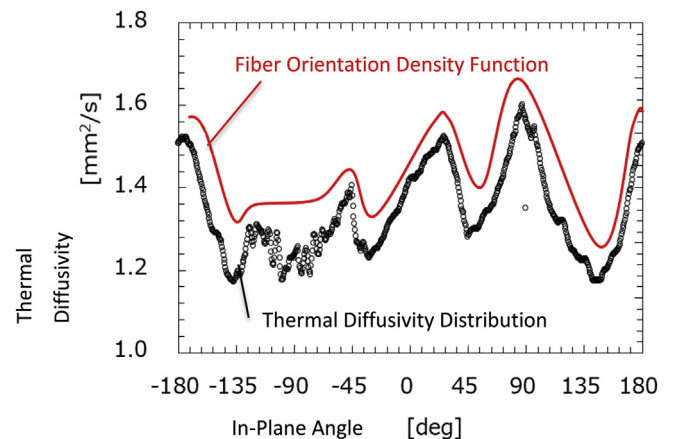


**Fig. 19.** Typical Measured Data of In-plane Thermal Diffusivity and Fiber Orientation Density Function obtained by Fitting.

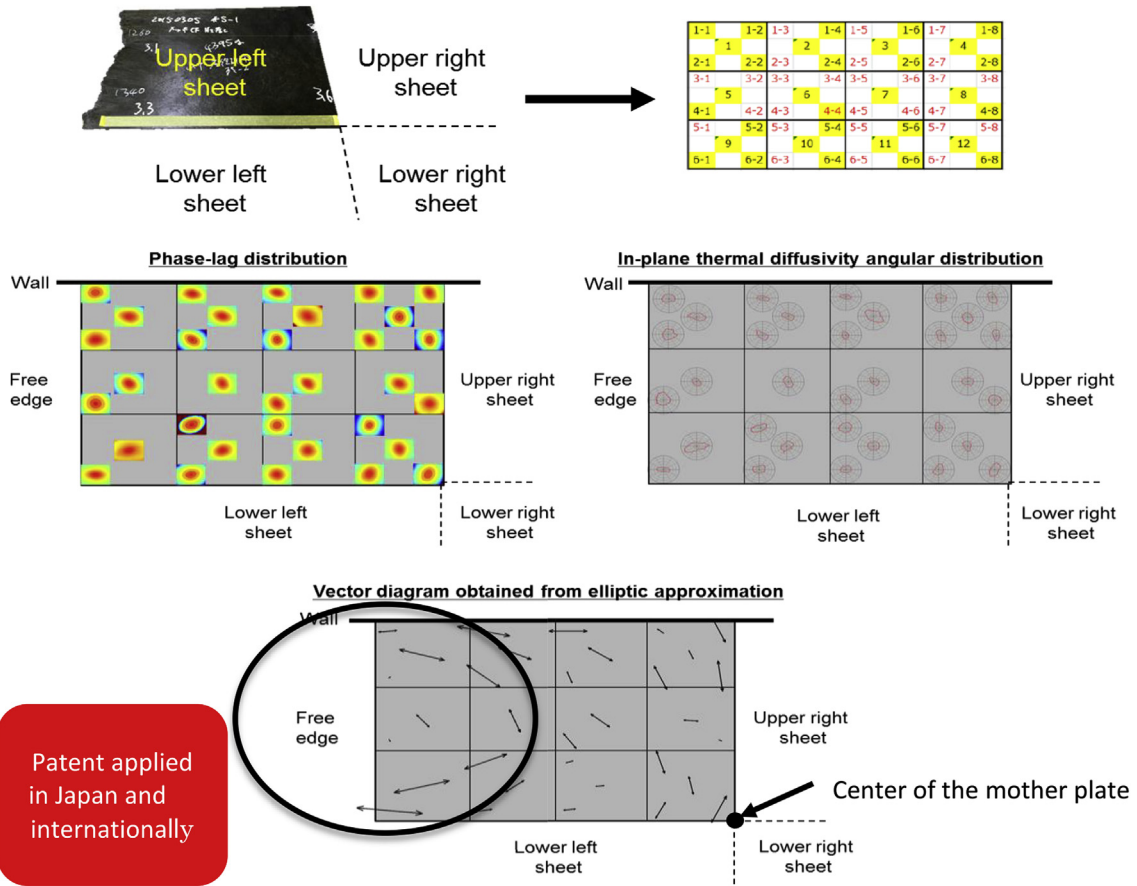


Fig. 20. Large high-speed hydraulic press of 3500 ton weight capacity installed in national composites center Japan in 2013: Key facility for LFT-d technology.

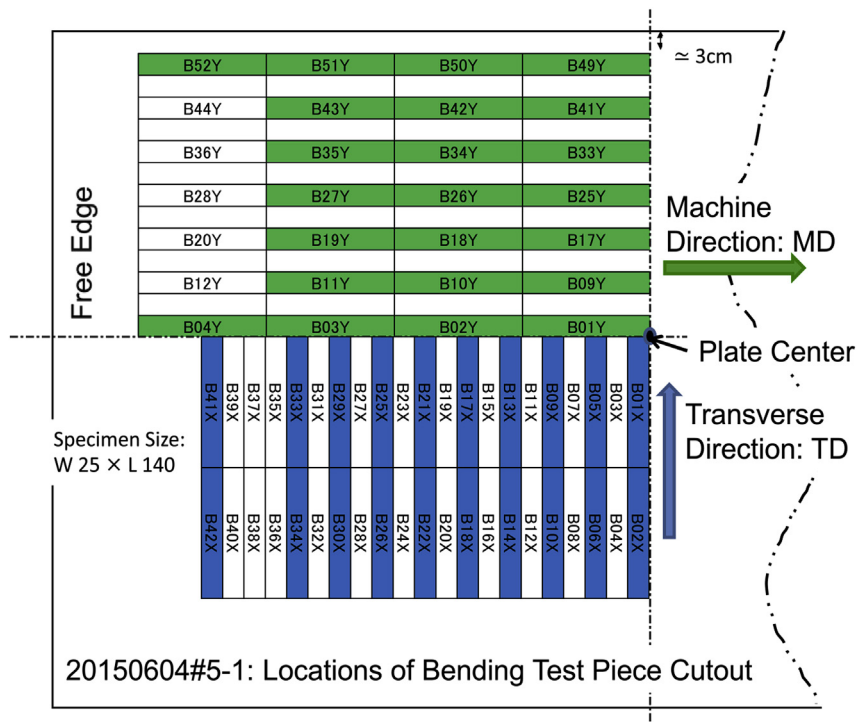


Fig. 21. Bending Specimen Cutout Map from the Large Mother plate of C-LFT-D.

mother plate fabricated based on the standard process parameters window in the early project phase (in FY2015) where the employed carbon fiber is Toray T700SC, the matrix is PA 6, and the fiber volume fraction ( $V_f$ ) is 30%. The distances between the plate center and the each specimen center are easily calculated. The marked specimens were subjected to bending tests in which the elastic modulus and strengths were determined. Figs. 22 and 23 describe the relationships between the distances between the plate center and each specimen center and normalized bending elastic moduli and tensile elastic moduli of the same plate as shown in Fig. 21, respectively. The employed value for normalization was the project target modulus defined at the project start and its absolute figure is closed. Although some anomalous data points can be found, some important trends in elastic moduli can be identified. For example, bending moduli in MD obtained from the specimens taken at far distant regions from the plate center are much larger than the bending moduli in TD. This finding is compatible with the measured fiber orientation direction and the intensity is indicated in the bottom of Fig. 18 so that a majority of discontinuous carbon fibers are aligned in the horizontal direction. In other words, an extent of the anisotropy is severe in the region indicated by a circle of the bottom of Fig. 20. On the other hand, the bending moduli in TD obtained from the specimens taken at near regions from the plate center are slightly larger than those in MD, except for some anomalous data. Again, this fact is compatible with rather vertical (parallel to TD) fiber orientation in regions near plate center as, indicated in the bottom of Fig. 20. Similar trends can be found in the tensile elastic moduli, although the probability of anomaly is slightly higher. Hence, the effects of discontinuous fiber orientations are very crucial upon the elastic moduli and importance of orientation information, by the fact and the prediction, can be well understood.

5.3. Strength properties

The behavior of the strength properties of LFT-D plate is essentially similar to elastic modulus properties, i.e., a strong dependency on the locations on the plate can be found. However, the other explanation in terms of the correlation between the elastic modulus and strength will provide a much better understanding of the strength behavior of LFT-D material. Fig. 24 shows a correlation between normalized bending moduli and normalized bending strengths for the same plate indicated in Figs. 21–23 and for another plate fabricated on the other fabrication trial date. The used

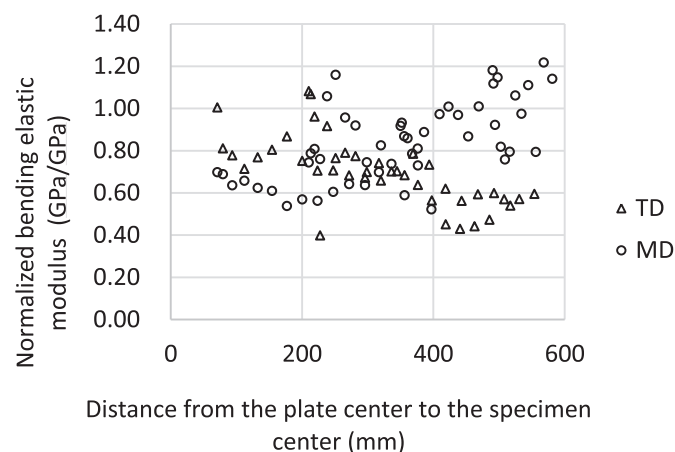


Fig. 22. Relationships between Normalized Bending Elastic Modulus and Distance from the Plate Center to the specimen Center.

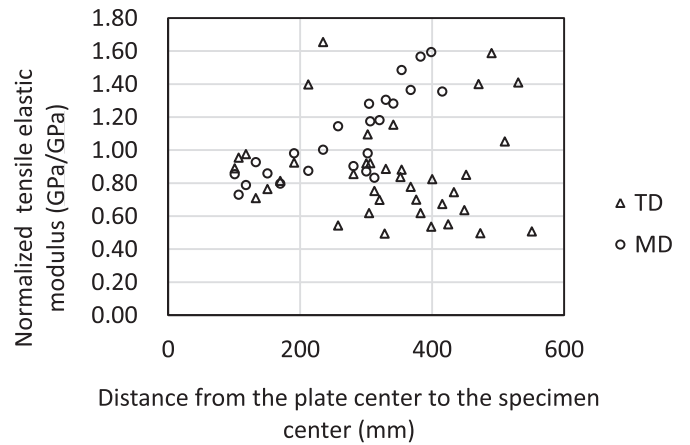


Fig. 23. Relationships between Normalized Tensile Elastic Modulus and Distance from the Plate Center to the specimen Center.

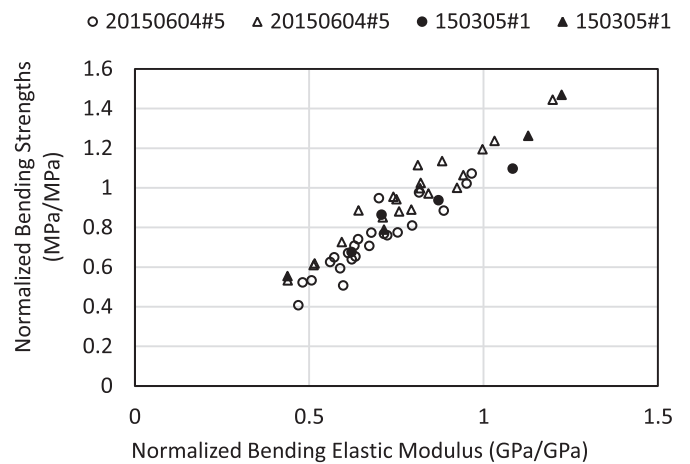


Fig. 24. Relationships between normalized bending elastic modulus and normalized bending strengths for LFT-d two mother plates.

value for normalization was the project target strength defined at the project start and its absolute figure is confidential. A very strong correlation between moduli and strengths can be seen in this figure. The fact derived from such strong correlation suggests a procedure of LFT-D structural design methodology based on predictions of fiber orientations by CAE. Efforts to establish the design methodology based on accumulated knowledge explained in this chapter are now undertaken in the project.

6. Carbon fiber LFT-D: viscoelastic properties of the products

6.1. Introduction

In this section, a measurement technique to obtain the thermo-viscoelastic properties of the LFT-D composites is discussed. A unidirectional compression creep test has been employed to measure the relaxation modulus of the LFT-D (Matrix: PA6, Fiber: T700SC Toray, Volume Fraction of Fiber: 30%), where a creep function derived by experimental creep test is approximated by a Voigt-viscoelastic model, then converted into a relaxation modulus expressed by a generalized Maxwell model. The temperature dependency of the relaxation moduli were expressed by shift factors based on the Arrhenius equation using activation energy.

## 6.2. Basic theory of thermo-viscoelasticity [34,35]

According to the linear-viscoelastic theory, a relation of stress history  $\sigma(t)$  and strain history  $\varepsilon(t)$  can be expressed by the Duhamel's convolution integral using a relaxation modulus  $E(t)$ :

$$\sigma(t) = \int_0^t E(t-\tau) \frac{d}{d\tau} \varepsilon(\tau) d\tau + E(t)\varepsilon(0) \quad (6.1)$$

where  $E(t)$  denotes the stress response when unit-step-like input of strain is applied at  $t > 0$ . Rewriting Equation (6.1) using a creep function  $J(t)$ , we have

$$\varepsilon(t) = \int_0^t J(t-\tau) \frac{d}{d\tau} \sigma(\tau) d\tau + J(t)\sigma(0) \quad (6.2)$$

where  $J(t)$  denotes the strain response when a unit-step-like stress input is applied at  $t > 0$ . Laplace transforms of Equations (6.1) and (6.2) are written as

$$\bar{\sigma}(s) = s\bar{E}(s)\bar{\varepsilon}(s), \quad \bar{\varepsilon}(s) = s\bar{J}(s)\bar{\sigma}(s), \quad (6.3)$$

where  $s$  is a parameter of the Laplace transform. The Laplace-transformed quantities are written with the over bar in the present paper. From Equation (6.3), we have a simple relationship between creep function  $J(s)$  and relaxation modulus  $E(s)$ .

$$\bar{E}(s) = \frac{1}{s^2\bar{J}(s)} \quad (6.4)$$

Consequently, we can obtain the relaxation modulus  $E(t)$  from the creep function  $J(t)$  by inversion of the Laplace transform of Equation (6.4).

In the present formulation, we use shear relaxation moduli  $G(t)$  and bulk modulus  $K(t)$  for the numerical computation based on a finite element method. The history of the bulk modulus of elasticity can be defined by the following equation with the instantaneous modulus  $E_0$  and Poisson's ratio  $\nu_0$  at the room temperature.

$$K(t) = K(0)H(t) = \frac{E_0}{3(1-2\nu_0)} H(t) \quad (6.5)$$

Namely, the bulk modulus is assumed to be constant without relaxation behavior. The Laplace transform of bulk modulus  $K(t)$  is given as

$$\bar{K}(s) = \frac{E_0}{3s(1-2\nu_0)} \quad (6.6)$$

Using  $E(s)$  in Equation (6.4) and  $K(s)$  in Equation (6.6), the Laplace transform of the shear relaxation modulus  $G(s)$  can be obtained as the following equation on the Laplace-transformed domain.

$$\bar{G}(s) = \frac{9\bar{K}(s)\bar{E}(s)}{3\bar{K}(s) - \bar{E}(s)} \quad (6.7)$$

Applying numerical inversion of Laplace transform, the shear relaxation modulus  $G(t)$  on the real time domain can be calculated.

## 6.3. Estimation of relaxation modulus [36,37]

### 6.3.1. Measurement of creep function of the LFT-D specimens

In order to obtain thermo-viscoelastic properties of LFT-D

(Matrix: PA6, Fiber: T700SC Toray, Volume Fraction of Fibers: 30%), we employed a unidirectional compression creep test as shown in Fig. 25. A square plate specimen (10 mm × 10 mm × 3.3 mm) are heated in the electric furnace and compressed in one axial direction using the loading weight, where the compression load was specified as 98.1 [N]. The testing temperatures were specified as 220, 230, 240, and 250 °C, respectively.

Fig. 26 shows histories of the displacements derived by unidirectional creep tests of LFT-Ds. In the present formulation, definitions of true strain and true stress were employed to avoid the estimation error of the creep function owing to the large deformation. At first, a definition of true strain of the following form is introduced to describe the deformation of the specimen.

$$\varepsilon(t) = \ln \frac{L(t)}{L_0} \quad (6.8)$$

where  $L_0$  is initial gage length of the specimen.  $L(t)$  is  $u(t) + L_0$ , where  $u(t)$  is a displacement history of the specimen.

Then, let us express the stress history  $\sigma(t)$  by the true strain  $\varepsilon(t)$ . In the state of large deformation, the alteration in volume of the specimen can be assumed to be relatively small, such that the cross-sectional area of the specimen can be approximately expressed by the following equation:

$$A(t) = A_0 \frac{L_0}{L(t)} = A_0 e^{-\varepsilon} \quad (6.9)$$

where  $A_0$  is the initial cross-sectional area of the specimen.

Discretizing the true strain  $\varepsilon(t)$ , true stress  $\sigma(t)$ , and creep function  $J(t)$  by  $\varepsilon_i$ ,  $\sigma_i$ , and  $J_i$  ( $i = 0, \dots, N$ ) for the time axis, a discretized finite differential representation of the convolution integral of Eq. (6.2) can be rewritten in the form.

$$\varepsilon_i = \sum_{k=1}^i J_{i-k} \left( \frac{\sigma_k - \sigma_{k-1}}{\Delta t} \right) \Delta t + J_i \sigma_0 \quad (6.10)$$

Namely, the discrete form of the creep function  $J_i$  can be calculated by the following recurrence equation from Equation (6.10).

$$J_i = \frac{\varepsilon_i}{\sigma_0} \sum_{k=1}^i J_{i-k} \left( \frac{\sigma_k - \sigma_{k-1}}{\Delta t} \right) \quad (6.11)$$

The creep functions of LFT-D are shown in Fig. 27.

### 6.3.2. Voigt model for approximation of creep function

A Voigt model is introduced to approximate the discrete creep functions obtained by unidirectional compression creep test. The generalized Voigt model has a serial structure composed of unit Voigt elements with a spring and damper, as shown in Fig. 28.

Here, an instantaneous elastic modulus  $E_0$  can be specified as Young's modulus  $E$  at room temperature; therefore, the instantaneous creep function  $J_0$  at  $t = 0$  should be  $1/E_0$ . The relationship between the elastic moduli  $E_0, E_1, \dots, E_n$  and a conclusive elastic modulus  $E_\infty$  at infinite time can be expressed as

$$\frac{1}{E_\infty} = \frac{1}{E_0} + \frac{1}{E_1} + \dots + \frac{1}{E_n} = \sum_{i=0}^n \frac{1}{E_i} \quad (6.12)$$

The creep function  $J(t)$  approximated by the Voigt model can be expressed as the following equation.

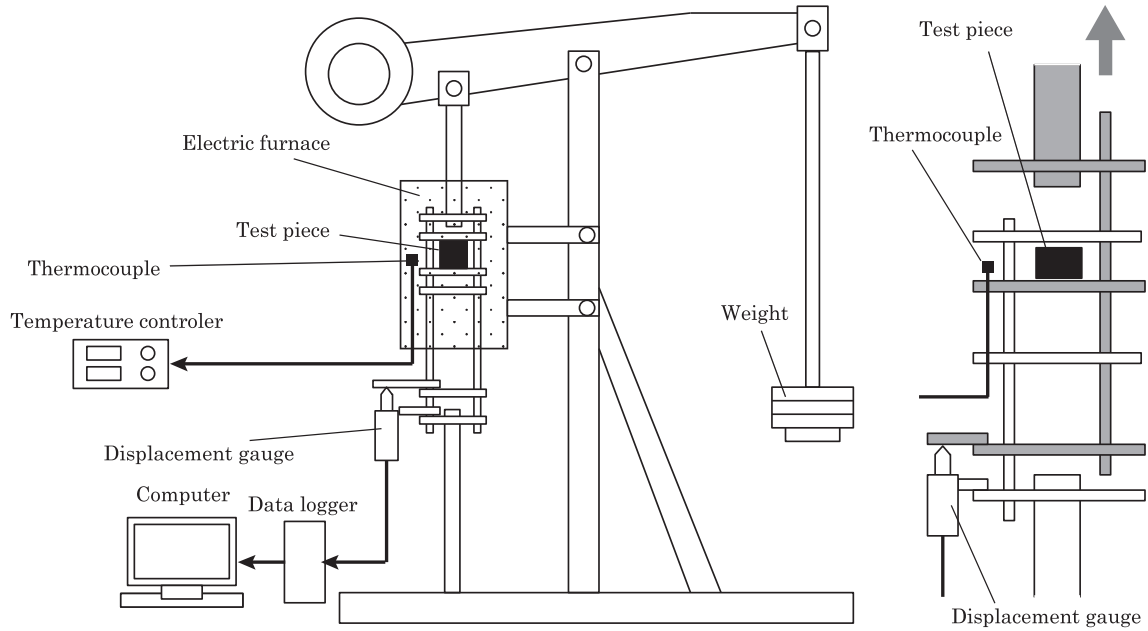


Fig. 25. Equipment of unidirectional creep test.

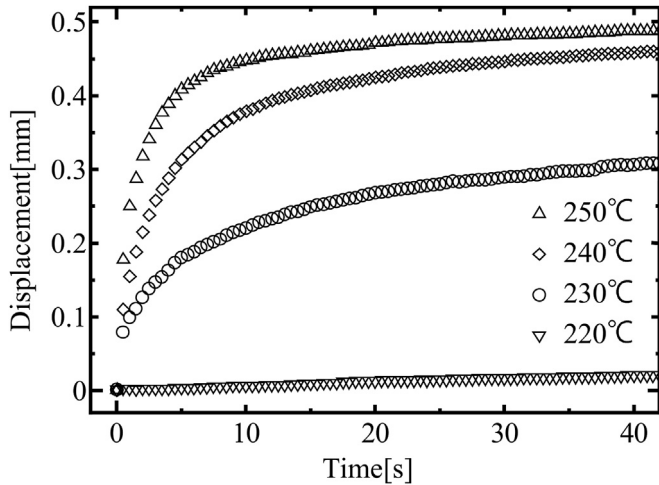


Fig. 26. Deformation histories derived by unidirectional creep tests of LFT-Ds.

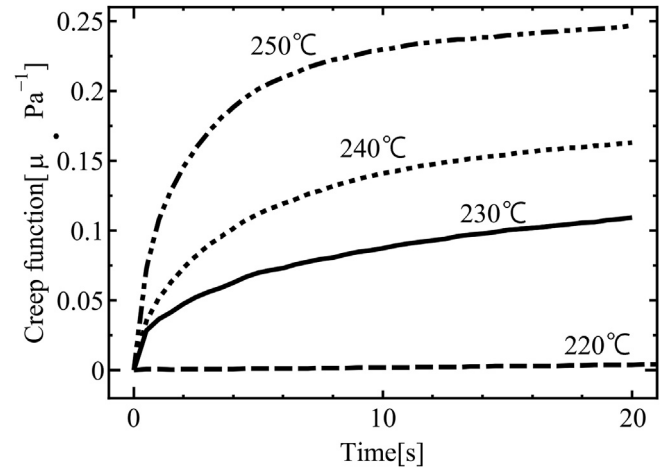


Fig. 27. Creep functions of LFT-Ds.

$$J(t) = \frac{1}{E_0} + \sum_{i=1}^n \frac{1}{E_i} \left\{ 1 - \exp\left(-\frac{t}{\tau_i}\right) \right\} \quad (6.13)$$

where  $\tau_i = \eta_i/E_i$ . In the present study, creep functions are approximated by the 3 unit Voigt model ( $n = 3$ ).

#### 6.4. Relaxation modulus

In order to calculate the relaxation moduli of LFT-D, the Laplace transform and Inverse-Laplace transform are introduced. From Equation (6.13), we have the Laplace-transformed creep function  $\bar{J}(s)$  as the following form.

$$\bar{J}(s) = \frac{1}{sE_0} + \sum_{i=1}^n \frac{1}{sE_i(1 + s\tau_i)} \quad (6.14)$$

Substituting Equation (6.14) into Equation (6.5) we have

$$\bar{E}(s) = \frac{1}{\left\{ \frac{s}{sE_0} + \sum_{i=1}^n \frac{s}{E_i(1 + s\tau_i)} \right\}} \quad (6.15)$$

As described before, a shear relaxation modulus  $G(s)$  on the Laplace-transformed domain can be calculated by substituting Equation (6.6) and Equation (6.15) into Equation (6.7). The relaxation moduli for LFT-D can be estimated by the Laplace transform of  $G(s)$  from Equation (6.7).

Consequently, the relaxation moduli of the LFT-D for 220, 230, 240, and 250 °C are shown in Fig. 29 with black solid lines. The red dashed lines in the figure are values approximated by the Maxwell model, as shown in Fig. 30. The Maxwell model used here is composed of five pairs of elastic ( $k_i$ ) and viscous ( $\eta_i$ ) elements and an infinite-time elastic element  $k_\infty$ . In this model, the shear relaxation modulus  $G(t)$  can be expressed as the form.

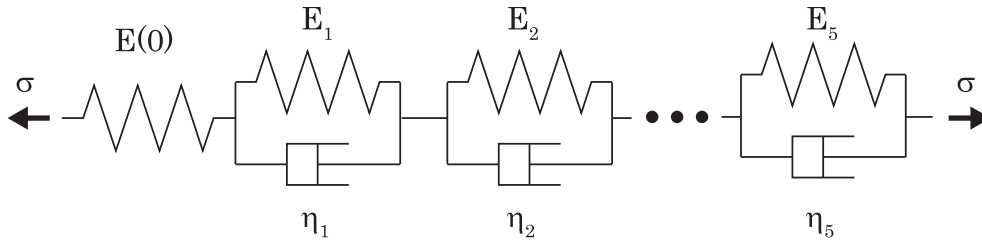


Fig. 28. Voigt model.

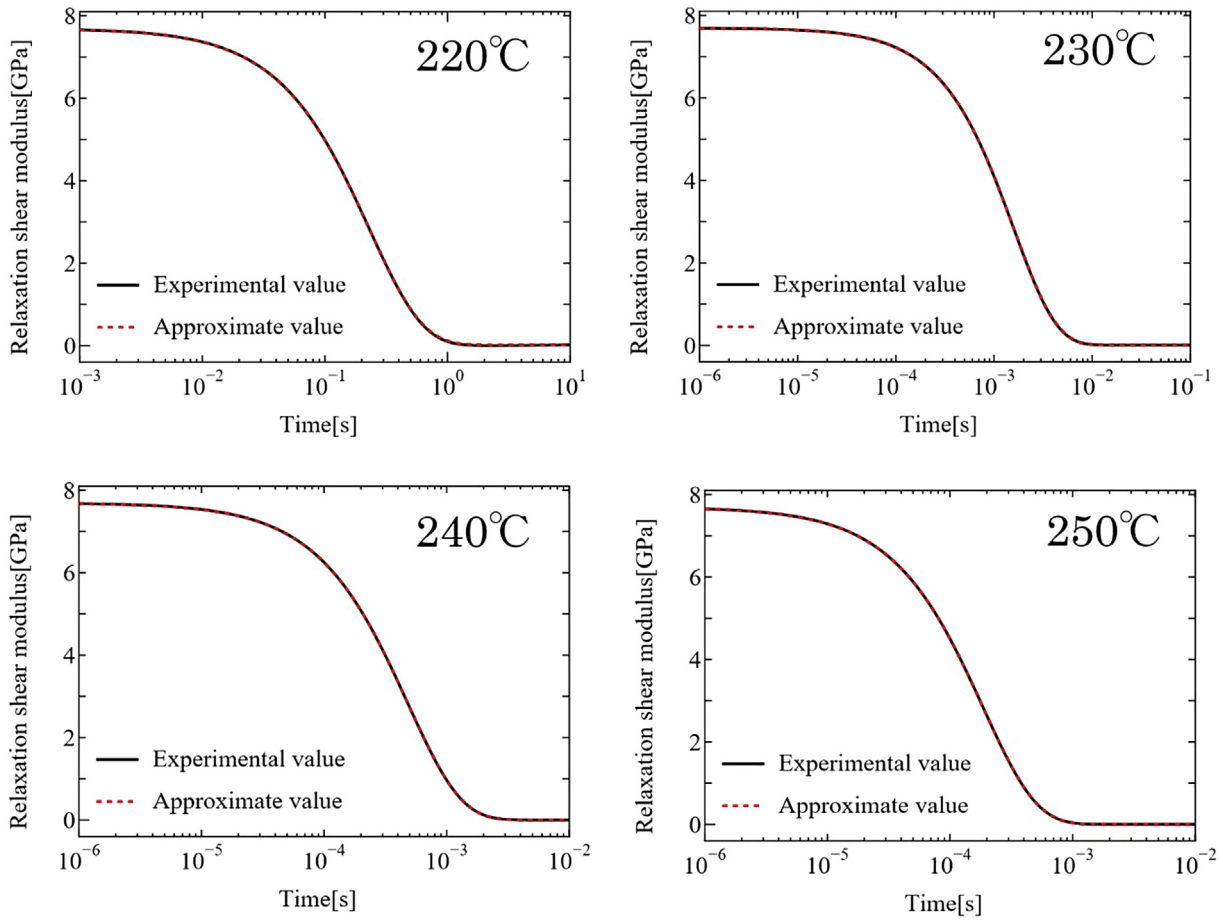


Fig. 29. Relaxation moduli of LFT-Ds derived by unidirectional creep tests.

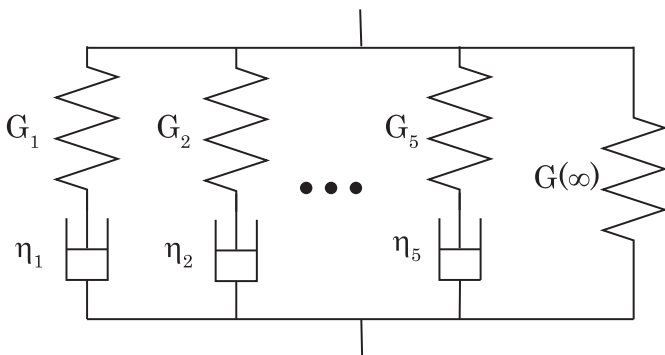


Fig. 30. Maxwell model.

$$G(t) = \sum_{i=1}^5 G_i \exp\left(\frac{-t}{\lambda_i}\right) + G_\infty \tag{6.16}$$

where,  $G_1, G_2, \dots, G_5$  and  $\lambda_1, \lambda_2, \dots, \lambda_5$  are unknown parameters ( $\lambda_i = \eta_i/G_i$ ). These parameters can be determined by an iterative calculation minimizing a residual function between relaxation modulus of Maxwell model with an assumed parameter  $G_i$  and that obtained by an experimental test. The estimated parameters  $G_i$  and  $\lambda_i$  of the Maxwell model for LFT-D are shown in Table 2. As shown in Fig. 31, it can be confirmed that the approximated values of the relaxation moduli with Maxwell model can be derived with very high accuracy.

**Table 2**  
Parameters of Maxwell model for each temperature of LFT-Ds.

Coefficient[GPa]	G1	G2	G3	G4	G5	G(∞)
220°C	3.07	2.30	1.53	0.460	0.307	0.0181
230°C	3.08	2.31	1.54	0.461	0.308	0.00308
240°C	1.90	1.90	1.90	1.90	0.769	0.00204
250°C	3.08	2.31	1.54	0.461	0.308	0.00138

Relaxation time[ms]	λ <sub>1</sub>	λ <sub>2</sub>	λ <sub>3</sub>	λ <sub>4</sub>	λ <sub>5</sub>
220°C	220	220	240	280	280
230°C	1.41	1.68	1.68	1.95	1.95
240°C	0.460	0.460	0.505	0.505	0.505
250°C	0.175	0.190	0.190	0.220	0.220

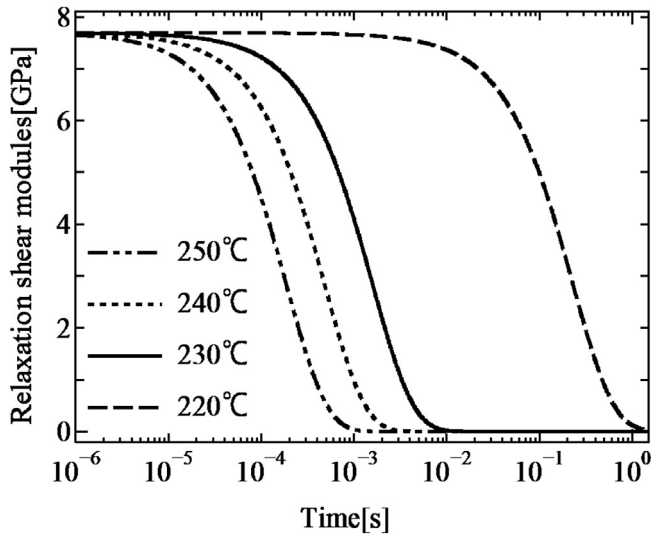


Fig. 31. Relaxation moduli for 220, 230, 240, and 250 °C of LFT-Ds.

6.5. Shift factor [38,39]

The relaxation moduli for the temperatures 220, 230, 240, and 250 °C are represented in Fig. 31. Taking logarithmic time for the abscissa axis of the relation moduli, the relaxation moduli at each temperature become almost the same profile, where the relaxation rate increase with temperature according to the thermo-viscoelastic theory. Namely, the effect of temperature can be expressed by a shift factor along the abscissa axis based on the standard relaxation modulus.

In the present study 220 °C is specified as the standard temperature. The relaxation modulus of the standard temperature is called a master curve. The shift factor  $\ln \alpha (T)$  is defined as a distance between the master curve and the relaxation modulus on the other temperature on the horizontal  $\ln t$  axis of the relaxation moduli.

The shift factors for each temperature are summarized in Fig. 32. Note that the horizontal axis of Fig. 32 is expressed by the inverse of the absolute temperature. In this graph, we can confirm that the shift factor  $\ln \alpha (T)$  and  $1/T$  indicates a linear relation partly. The slope of the relation for  $\ln \alpha (T)$  and  $1/T$  changes with the standard temperature 220 °C. In the present strategy, the shift factor  $\ln \alpha (T)$  was an approximated Arrhenius equation of the form,

$$\ln \alpha(T) = \frac{\Delta H}{R} \left( \frac{1}{T_0} - \frac{1}{T} \right) \tag{6.17}$$

where,  $R$  is the gas constant ( $= 8.31 \text{ J/mol K}$ ),  $T_0$  is the standard

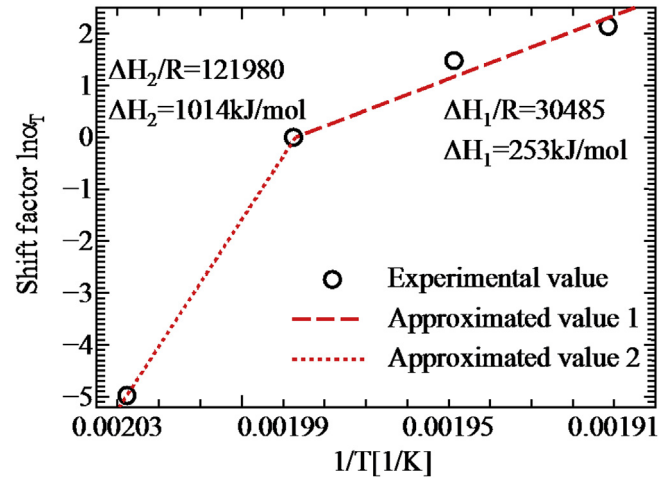


Fig. 32. Shift factor of LFT-Ds.

temperature (293 K). The activation energy  $\Delta H_1$  (Over 293 K) was estimated as 253 kJ/mol and  $\Delta H_2$  (under 293 K) was estimated as 1014 kJ/mol. The master curve of Maxwell model, namely the parameter of the Maxwell model and shift factor can be determined; the viscoelastic deformation of the LFT-D can be calculated by the standard finite element programs like ABAQUS [40], ANSYS [41], MARC [42], LS-DYNA [43], and so on. In these FEM codes, the Maxwell model or Prony series model (which is equivalent to Maxwell model) can be used for the structural analyses. For the shift factor, nearly all FEM codes support an Arrhenius-type model or WLF-type [44] model. Even when the FEM software does not have an Arrhenius model's shift factor, you can use it by including adequate user subroutines.

Using a viscoelastic model, we can calculate the behavior of press molding [45], residual stress in the curing process [46], creep deformation [47] of the LFT-D, and other viscoelastic materials using universal FEM codes. Since the present viscoelastic model is a linear model supposed to be small deformation, it cannot be applied in the “nonlinear” cases. In the case of nonlinear problems of viscosity, we have to take into account the strain rate dependency of the coefficient of viscosity. On the other hand, when strong nonlinear stress/strain relation appears, owing to the plastic deformation, the nonlinear model based on viscoelasto plasticity should be used.

7. Carbon fiber LFT-D: ultrasonic fusion bonding technique

7.1. Background and outline of ultrasonic fusion bonding method

Although each component of the chassis can be well fabricated, several joining technologies of LFT-D components must be established to assemble the whole chassis. As joining technologies, fusion bonding, adhesive bonding, and mechanical fastening are considered in the project. In order to promote the advantage of thermoplastic composites, fusion bonding technology was considered as the most important target to be developed. Among several methods of the fusion bonding, ultrasonic fusion bonding, laser bonding and induction heating welding were pursued in the first phase of the project. However, the induction heating welding was discarded first because the establishment of conditions was very difficult owing to discontinuities and rather low volume content of carbon fiber in the case of LFT-D. Although a laser bonding method is not impossible to apply, several barriers were identified to apply it practically. Thus, ultrasonic fusion bonding was chosen as the

most appropriate method, partly because only the regions near contact faces of two pieces can be melted if ultrasonic fusion bonding conditions such as input energy are given properly.

The concept of the ultrasonic fusion bonding and a photograph of the designed bonding jig for preparing test pieces are shown in Fig. 33 [48]. In the bonding machine used here, an alternating electrical oscillation signal of 15.15 kHz is generated first and it is converted into mechanical vibration of the same frequency by a piezoelectric element in the machine, i.e., ultrasonic vibration generation. This vibration is introduced to a surface of one piece to be bonded through a horn and it is finally converted into heat at the reverse contact surface between two pieces. If the given conditions of the vibration are proper, the converted temperature becomes high enough to melt thermoplastic material around the contact surface in less than 1 s. Thus, the ultrasonic fusion bonding can be achieved by an appropriately designed bonding or welding machine. The developed know-how in this project [48] was an application of some polymer film, such as “Kapton,” to an upper surface of the piece for averaging incident mechanical vibration energy. A concept of the actual operation procedure of the machine used here is indicated in Fig. 34. The level of the oscillation trigger load is of the order of 1 kN and the level of the prescribed energy ( $\int W ds$ ) is of the order of some hundreds to thousands of Joules for LFT-D bonding.

## 7.2. Evaluation of the mechanical properties of ultrasonic fusion bonded plates

The first object to be bonded was the double cantilever beam (DCB) specimen for the evaluation of mode I interlaminar fracture toughness of ultrasonically fusion bonded region of LFT-D plates of 3 or 4 mm in thickness. The width of the specimen was defined as 25 mm and the length was approximately 140 mm. Three types of fusion bonding conditions were chosen: as-is, energy director provision (ED), and Polymer string provision (PS). The basic dimensions and explanation of the specimen types are shown in Fig. 35, where one ED ridge height is 0.5 mm and it is prepared by pressing using a grooved mold surface and a polymer string of PA6 with approximate diameter 0.5 mm. A square-shaped horn head of length 10 mm was chosen and six steps of bonding were performed with no gap arrangement, as shown in Fig. 35 [48]. Initial crack starter was prepared by placing a 25 mm by 20 mm Kapton tape

between two bonded pieces. Glued specimens (GL) using common epoxy adhesive (Araldite<sup>®</sup>) and polycyanoacrylate (Alon Alfa<sup>®</sup>) adhesive were also prepared as reference data. Examples of ultrasonic nondestructive evaluation results of fusion bonded and glued specimens are indicated in Fig. 36 [48] where the percentage numbers describe the relative bonded area ratios to dotted rectangles in each specimen. It can be seen that fusion bonding with ED cases show the highest bonding ratio among all cases. For the evaluation of Mode I interlaminar fracture toughness of bonded specimens, a basic area method was employed and its description is shown in Fig. 37. As shown in this figure, the first crack propagation takes place at the load  $F_{(\delta)}$  and the load drops to  $F1_{(\delta)}$  (from Point A to B), where the crack tips grows from  $a$  to  $a_1$ . The released energy in this phase can be written as:

$$U_1 = \int_0^{\delta_1} (F_{(\delta)} - F1_{(\delta)}) d\delta \quad (7.1)$$

The energy release rate at this first crack growth step,  $G_{I1}$ , can be simply calculated as:

$$G_{I1} = U_1 / [(a_1 - a)b] = U_1 / A_1 \quad (7.2)$$

where  $b$  is the width of the specimen and  $A_1$  is an increased area of the crack by its growth. In Equation (7.1), the force function  $F1_{(\delta)}$  can be assumed as a linear function of deflection  $\delta$  on a line OBC, and it can be written as follows:

$$F1_{(\delta)} = \left( F_{(\delta_1)} / \delta_1 \right) \cdot \delta \quad (7.3)$$

At the next crack growth step, the corresponding energy release rate  $G_{I2}$  can be similarly calculated. The reason the area method was employed was that this method is versatile to calculate an energy release rate when stick-slip phenomena in DCB tests occur frequently [49]. Fig. 38 [48] indicates two typical cases of load vs. deflection curves obtained by DCB tests where stick-slip phenomena are dominant and where gradual crack growth is dominant. The former cases show the lower maximum loads and wide crack area growth at one step. The latter cases show the higher maximum load and narrow crack area growth at one step. In the latter cases,

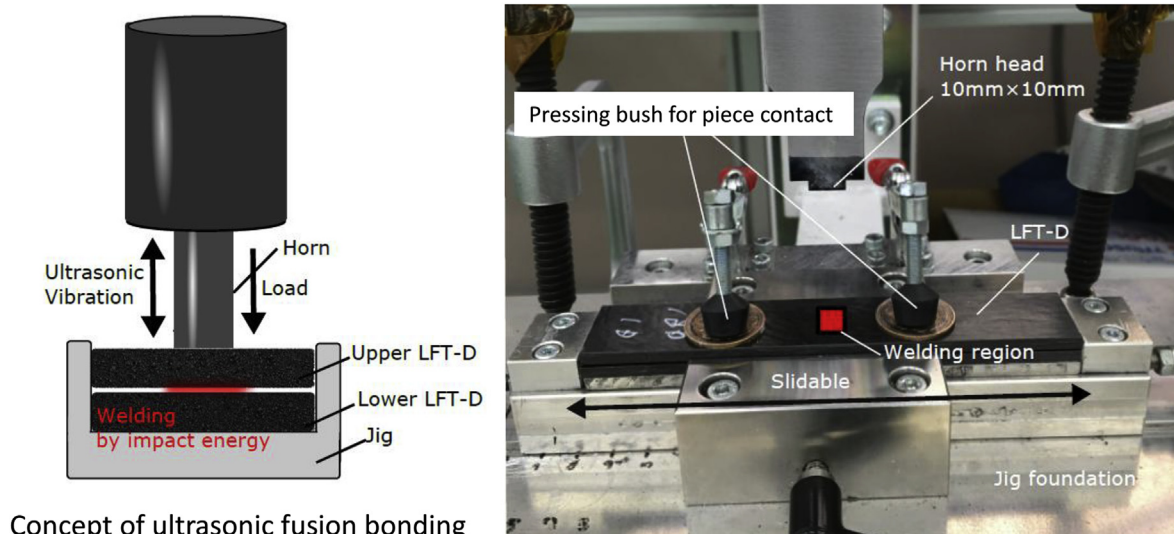


Fig. 33. Concept the ultrasonic fusion bonding method and photo of the designed jig for specimen bonding.

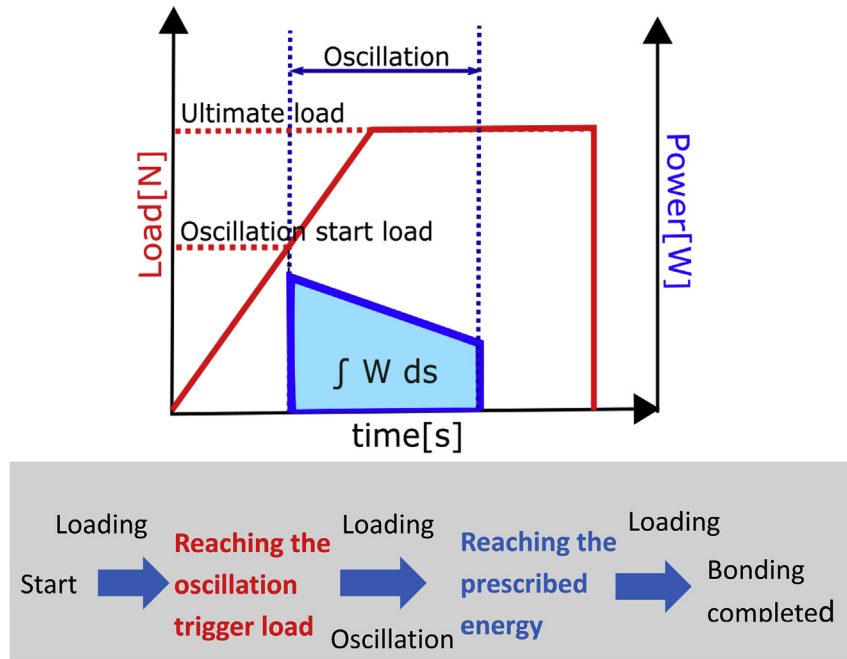


Fig. 34. Concept of the actual ultrasonic fusion bonding operation in the case of the machine used in this project.

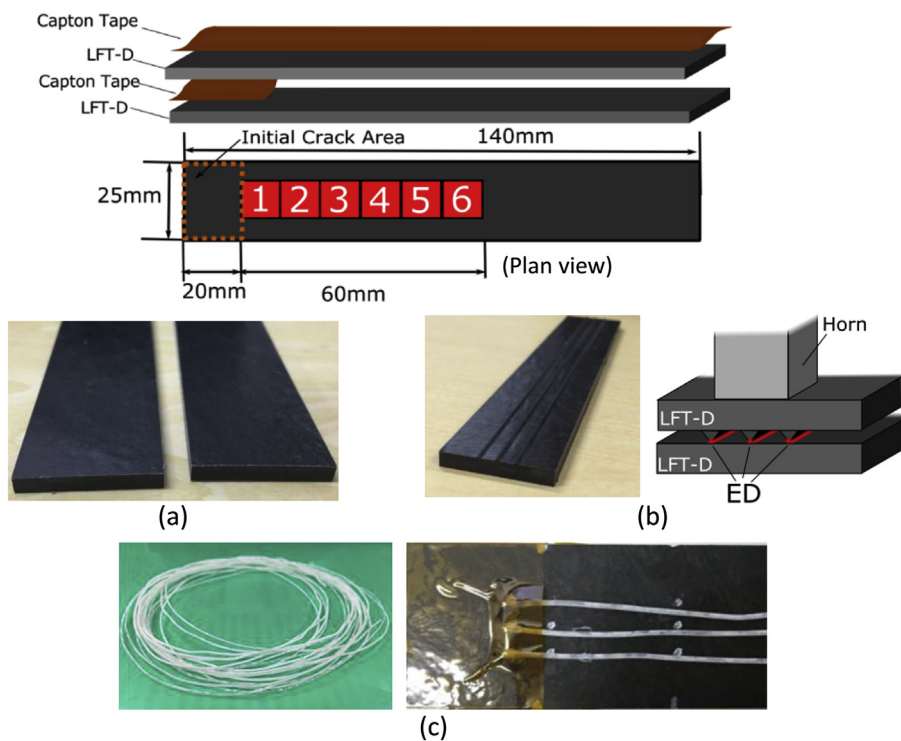


Fig. 35. Dimensions of DCB specimens for fracture toughness evaluation of fusion-bonded LFT-D pieces and three types of fusion bonding cases.

bending failure sometimes occurs prior to intended crack growth lengths, owing to low bending strengths compared to the high peeling strengths. By applying the equations explained above, interlaminar fracture toughness data at each crack growth step can be obtained. Fig. 39 [48] concludes the averaged fracture toughness data for the three types of fusion-bonded and two types of glued specimens (i.e., for seven specimens) at crack onset and 20 mm

crack growth. Although wide scatters in the data are observed, fusion-bonded cases with ED provision show the highest fracture toughness. Fusion-bonded cases in the As-is state show slightly lower toughness data. It can be seen that toughness results of the glued specimens are significantly lower than those of fusion-bonded specimens, even for the PS specimen cases. The superiority of fusion bonding for LFT-D structure joining can be well

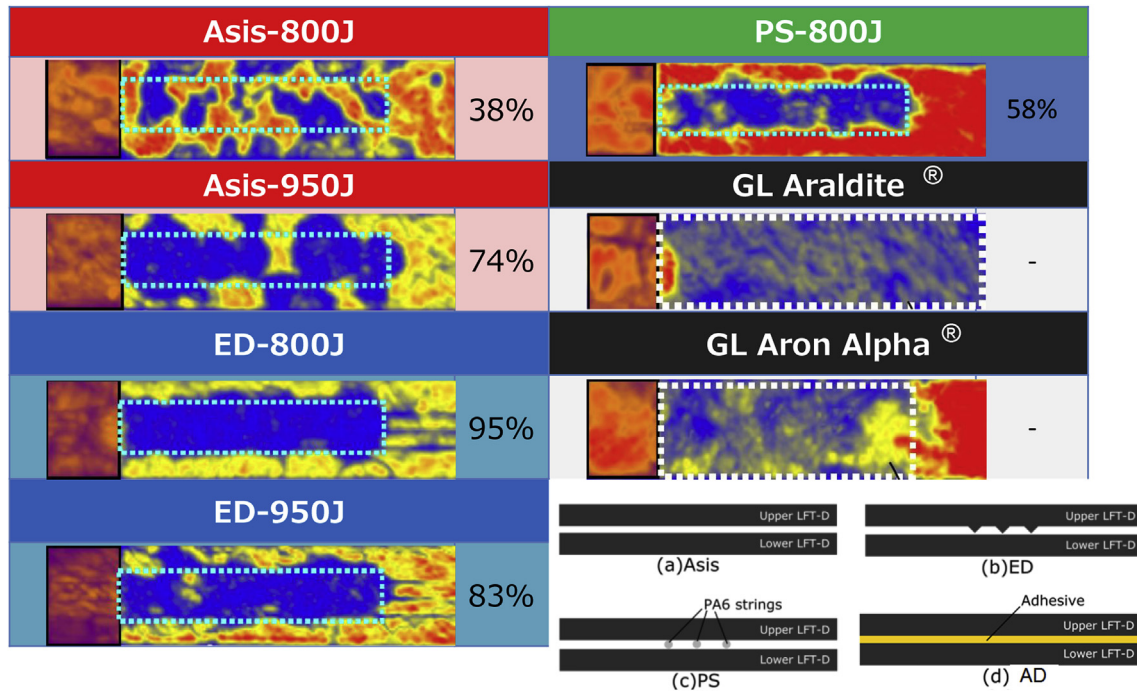


Fig. 36. Ultrasonic C-scanning images of typical DCB specimens for three types of fusion-bonded specimens and glued specimens, and schematic of specimen sections.

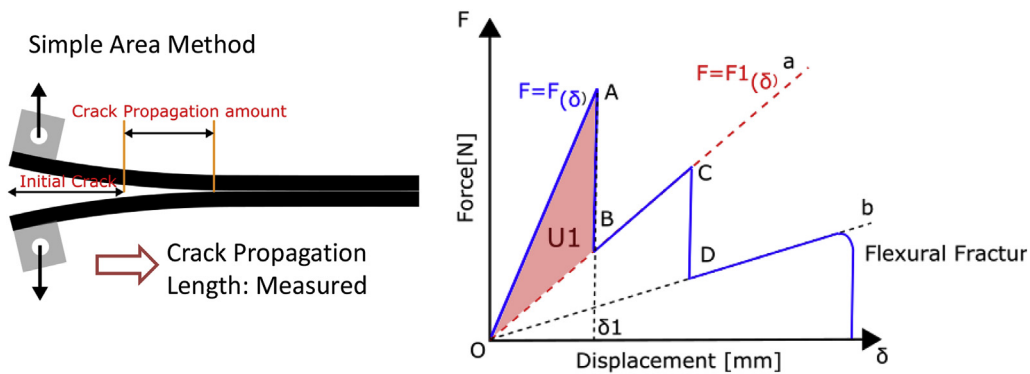


Fig. 37. Explanation of basic area method when stick slip behavior occurs in DCB test.

demonstrated in this part of the research.

Another mechanical property to be measured should be the single-lap shear strength of ultrasonic fusion bonded plates, which is practically conducted to evaluate bonding performances. The specimen size and concept are indicated in Fig. 40, where one shot of fusion bonding is applied to the center of a 25 mm square region. The glued specimens were not subjected to this single lap shear test. Owing to the low tensile strengths of LFT-D plates, tensile failure can occur prior to the intended lap shear failure if this shear strength is somehow high. The failure mode and corresponding number of the specimens are indicated in each column in Fig. 41 [48]. The tests results are indicated as failure loads in Fig. 41. If fusion bonding energy increases, the probability of tensile failure also increases. Although the indication is omitted, the lap shear strength values, the failure load divided by the true bonded region determined by ultrasonic C-scan images, range from 15 to 20 MPa, which are considerably high values for an initial phase of bonding technology development.

## 8. Outline of automotive composites technology development conducted in the University of Tokyo

The University of Tokyo had organized Japanese project of CFRTMP for mass production automobiles from 2010 to 2014 [50,51]. Then, a new and larger project with thirteen companies, including two CF manufacturers, four automotive manufacturers, six universities, and three public institutes started from 2015 (project leader is Prof. Jun Takahashi of the University of Tokyo) [52,53]. As shown in Fig. 42, continuous and discontinuous thermoplastic intermediate materials, structural optimization, high-cycle molding and jointing, and closed-loop recycling have been in development.

### 8.1. Continuous and discontinuous thermoplastic intermediate materials and closed-loop recycling

The weak point of continuous FRP is a formability for complex shaped components. On the other hand, the mechanical properties of conventional discontinuous FRP are too poor to use as structural

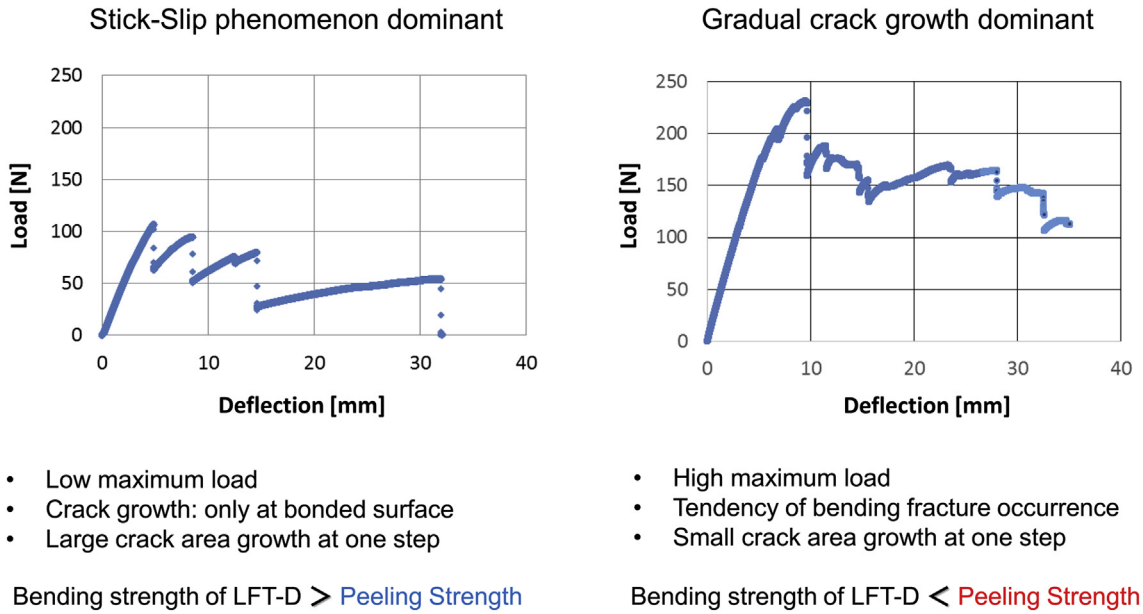


Fig. 38. Typical load vs. deflection relationships in DCB tests of ultrasonic fusion-bonded plate specimens.

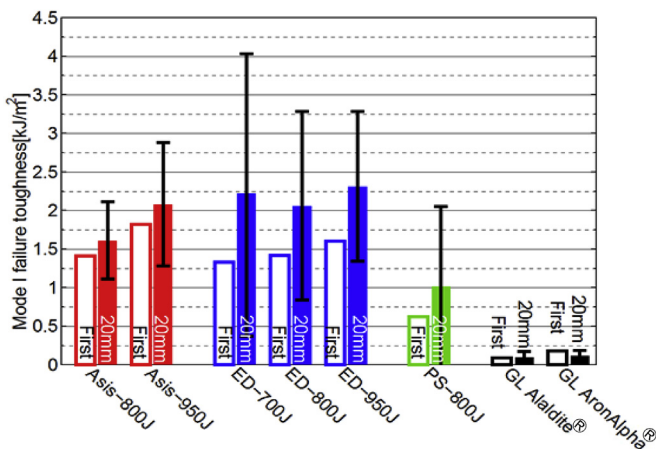


Fig. 39. Results of Mode I fracture toughness obtained by DCB tests for three types of fusion-bonded and two types of glued specimens of LFT-D plates: averaged data at crack onset and at 20 mm crack propagation.

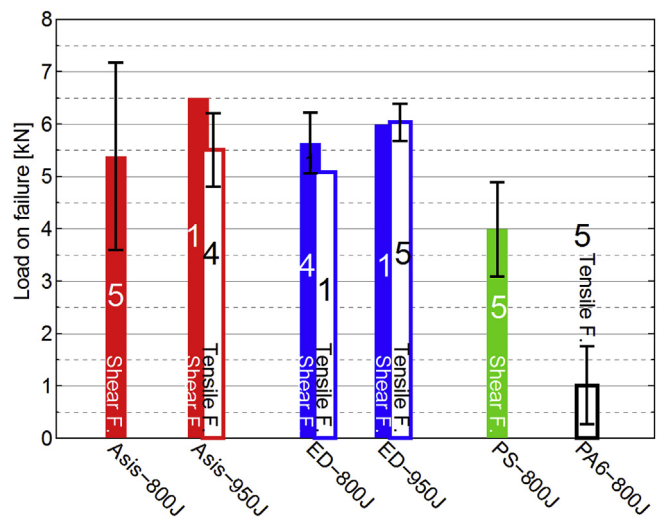


Fig. 41. Results of lap shear strength tests in failure loads for three types of fusion-bonded LFT-D specimens and neat PA6 resin specimens: averaged data (if not single datum) for indicated failure mode and numbers of specimens in each column.

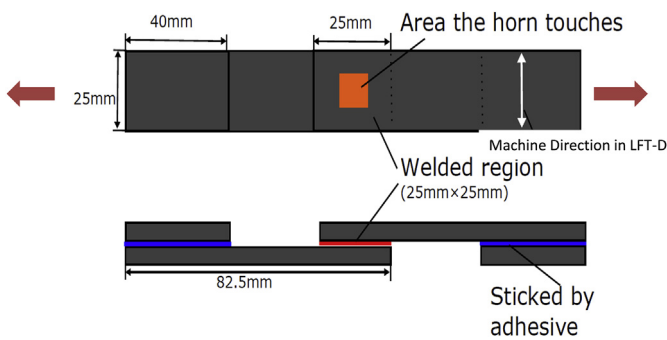


Fig. 40. Specimen size and dimensions for single-lap shear tests for ultrasonic fusion bonded LFT-D plates.

components of an automobile. Therefore, we intend to develop discontinuous thermoplastic intermediate materials, keeping both

CF linearity and sufficient aspect ratio to realize high-performance, affordable, formable, and recyclable components, as shown in Figs. 43 and 44.

One of them, chopped carbon fiber tape reinforced thermoplastics (CTT) made of resin-impregnated unidirectional thin CF tapes whose thickness is less than one third those of conventional tapes, realized superior mechanical properties with small scatter (Fig. 45) [54–60]. Additionally, thanks to the tape thinness, the resin-impregnation speed becomes ten times faster than with conventional products, and thanks to the small tape dimensions, a low-cost papermaking technique can be applied for tape dispersion. As a result, it became possible to dramatically reduce the cost of manufacturing prepregs other than CF cost and molding cost.

In the case of closed-loop recycling which means that recycled CF will be used to make automotive members again, there are concerns about both degradation of recycled CF during the resin

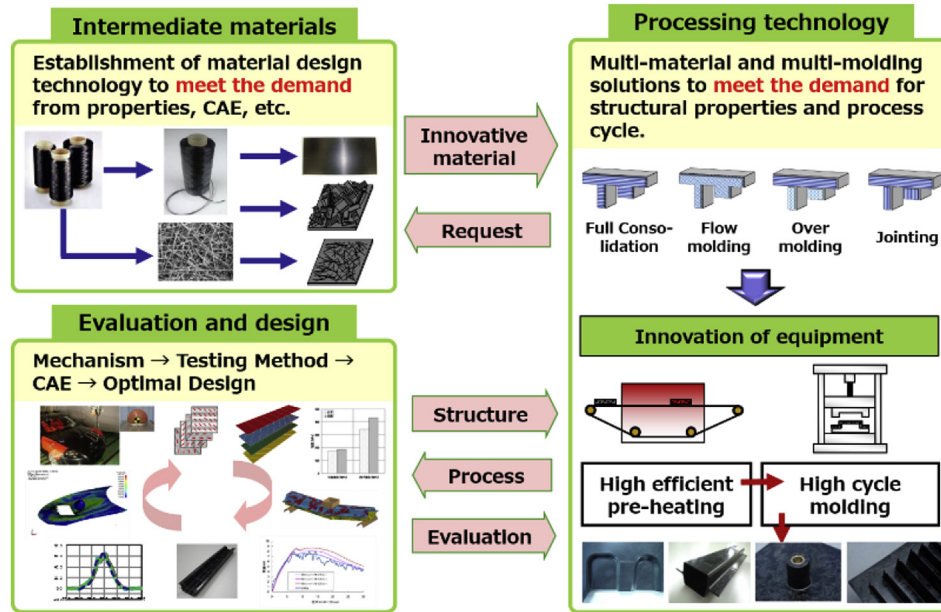


Fig. 42. Research topics in the Japanese automotive CFRTP project organized by the University of Tokyo, Japan since 2015.

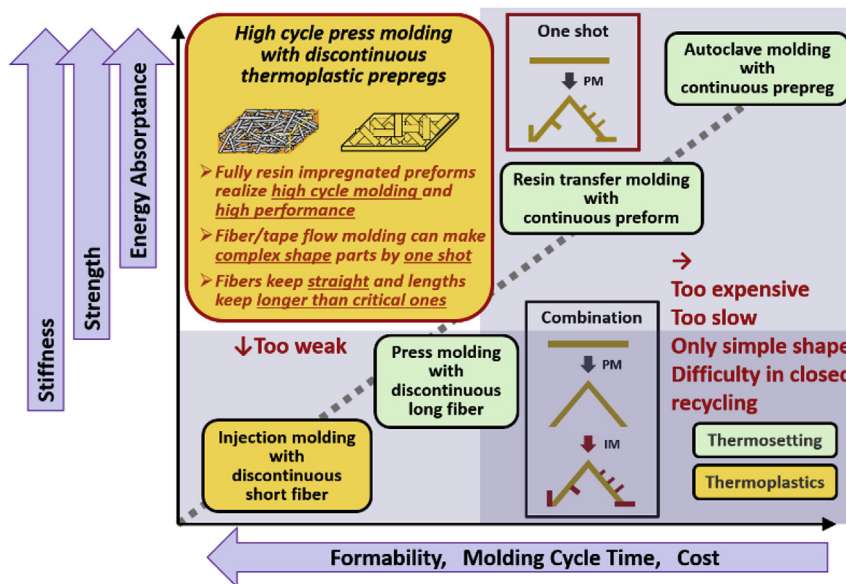


Fig. 43. Development direction of CFRTPs in the project to realize high-performance, affordable, formable, and recyclable components.

removal process and regeneration of functional groups for an adhesion with thermoplastics to make CFRTP again [61–63]. Therefore, we selected a superheated steam treatment method, which is not only low-cost but also able to sensitively control the CF degradation and add functional groups simultaneously [64].

One of the other intermediate materials, two types carbon fiber mat reinforced thermoplastics (CMT), which are produced by a paper making method or carding method, is a suitable application of the recycled CF, and the CMT show excellent mechanical properties with small scatter even in the case of recycled CF [65,66].

8.2. Structural optimization for further weight lightening

The flowability of discontinuous CFRTP allows a mass

production of “variable thickness structure”, which enables a wide range of practical applications including large structural components, such as automotive floors. Such a variable thickness CFRTP panel is shown to be 16% lighter than flat CFRTP panel, and hence 74% lighter than flat steel panel with the same flexural stiffness [67,68].

Additionally, in the case of laminated FRP, there is a design restriction that corner radii have to be bigger to avoid delamination. This is because delamination causes lower structural strength than that expected by the tensile and compressive strength of the employed material. CFRTP with a polypropylene or polyamide matrix allow smaller corner radii, thanks to their mechanical properties, which makes the design more flexible and the structure stiffer [69,70].

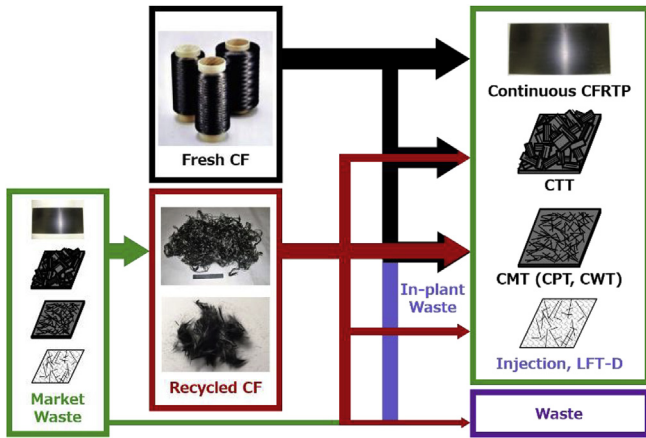


**Fig. 44.** Developing intermediate materials in the CFRTCP project: chopped carbon fiber tape reinforced thermoplastics (CTT), carbon fiber mat reinforced thermoplastics (CMT), carbon fiber paper reinforced thermoplastics (CPT, see Fig. 5(a)), and carbon fiber card web reinforced thermoplastics (CWT).

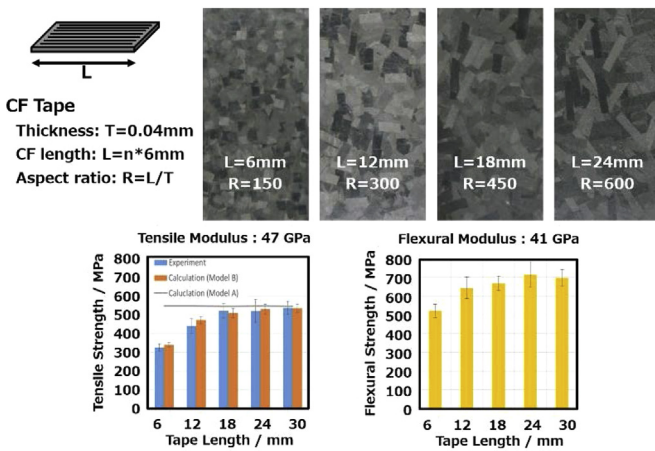


**Fig. 45.** Tape length dependence on the tensile and flexural strengths of ultrathin chopped carbon fiber tape reinforced thermoplastics (UT-CTT).

**8.3. Functional design**

CFRTCP are generally expected to exhibit a high-energy absorption capacity and thermoforming ability. However, thanks to the ductility of the matrix resin, both soft skin effect, which contributes pedestrian safety [71], and higher residual mechanical properties after lightning strike [72–74] are proved as attractive features. Additionally, foamed material with both superior lightweight and heat/sound insulation properties has been investigated as an application of CF-paper-reinforced thermoplastics (CPT, see Fig. 46) [75].

**8.4. Molding and nondestructive inspection**

Before developing a molding method using the developed intermediate materials, a harmful volume fraction of void had been investigated [76]. Then, we have been developing high-cycle molding methods (Fig. 47) to realize both smaller void content than this harmful value and excellent reproducibility of mechanical properties. Additionally, a nondestructive inspection method to detect the harmful void by using soft X-rays has been developed, which can be used in an actual production line [77–79].

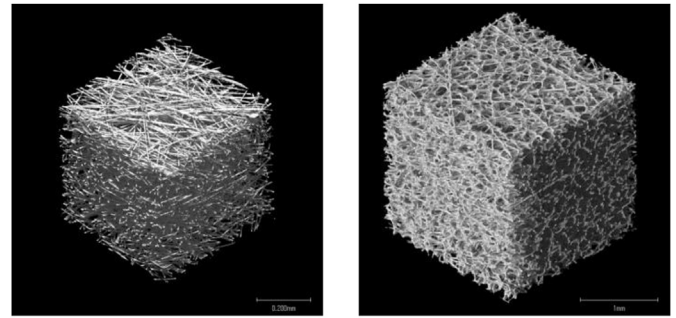


**Fig. 46.** SEM images of CPT (a) and carbon fiber reinforced thermoplastic foam (CFRF) (b).

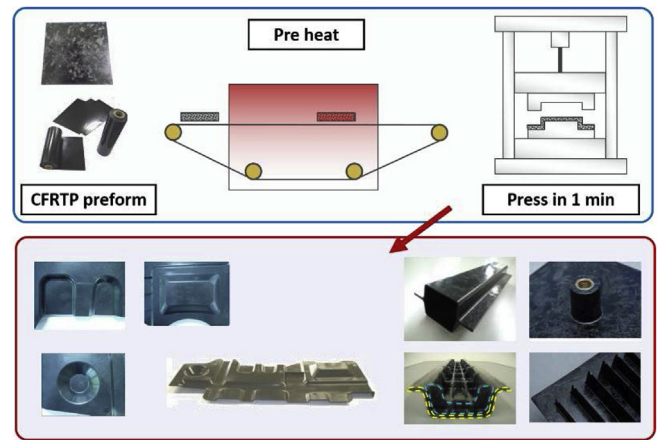


**Fig. 47.** Schematics of developing high-cycle compression molding for mass production automotive components.

**9. Conclusions and future prospects**

CFRP applications to automotive structures have been rapidly expanded, particularly by European automotive manufacturers in recent years. As explained, a strong incentive to apply CFRP to automobiles essentially comes from regulations for CO<sub>2</sub> emission reduction per unit distance. Among these, the regulation called EURO 6 will be applied in 2020, resulting in significant taxes being levied on vehicles exceeding 95 g/km of CO<sub>2</sub> emission, by a resolution of the European Union. This is the reason European car manufacturers have been very keen to develop new technologies for CO<sub>2</sub> emission reduction. Weight reduction of automotive structures is one of the very efficient means to reduce their CO<sub>2</sub> emission. Some statistical data tell us that 100 kg weight saving in a car leads to 20 g/km CO<sub>2</sub> emission reduction. Thus, the effort to realize lighter-weight cars has recently become a serious challenges for automotive industries. Applications of CFRP are the most powerful route to reduce car weights. Unfortunately, Japan's efforts to apply CFRP to automobiles are far behind to those levels in Europe. In this article, Japan's national class effort to apply CFRP based on a thermoplastic matrix (CFRTCP), particularly discontinuous carbon fiber reinforced thermoplastic composites, has been reviewed. The basic technology adopted here is the so-called LFT-D, originally developed in the Fraunhofer Institute in Germany using glass fiber. The project has been performed in the NCC Japan established in Nagoya University. C-LFT-D has been tackled in these five years and some remarkable automotive components were

successfully fabricated recently. In parallel to this activity, one alternative technology of discontinuous carbon fiber reinforced thermoplastic composites has been developed by the University of Tokyo group. Their current status and important results have been also reviewed in this article.

The project outline in NCC is explained first, where its goal is to replace all components of a current aluminum alloy chassis by C-LFT-D components with slightly lighter weight ( $\Delta 10\%$ ) and the same rigidity as the baseline aluminum chassis. As the baseline car, a “Lotus Elise” was selected because the full chassis of this car was already made of aluminum alloy. Regarding a production tact time of C-LFT-D components, 1 min was defined as the target. As a matrix thermoplastic resin, PA6 was adopted so far in this project. This resin is supplied to the first axis of the extruder and continuous CF bundles are supplied to a certain portion of the screw of the extruder second axis. The CFs are cut or broken into short fibers and blended with melted resin, and extruded from a nozzle. The extruded material is called “Futon” in NCC Japan, which originally means a cotton mat of Japanese foldable bed. Because temperature of “Futon” rapidly goes down after extrusion, a temperature control chamber was placed just after the extruder. Additionally, a material handling system composed of a fast moving robot and a special end effector with a heat keeping system was developed and used in NCC. The compaction speed of the press is a very important parameter consisting of a process window of LFT-D. A hybridization of LFT-D with continuous fiber CFRTP prepreg of the same matrix has to be developed for higher-rigidity components and this process was rather easily completed. Several kinds of chassis components have already been successfully fabricated. Among these, the most difficult was a floor panel of 2 m<sup>2</sup>, the largest component of the chassis, and the second most difficult one was a side sill inner requiring a hybrid processing using a fabric (twill) prepreg with the same PA6 matrix as LFT-D. The obtained optimization results describe significant variation in thickness corresponding to side sill locations. For LFT-D processing technology, it is very easy to fabricate such a variation of thickness. This point is a great advantage of the LFT-D processing technology. The assembly of the whole chassis made by LFT-D with continuous fiber textile prepreg will be completed in the spring of 2017.

The prediction of fiber length distribution is a very important scientific element of the project. A new function was proposed and its theoretical essence is explained in Section 3.1. From an experimental point of view, the establishment of measurement methods of fiber length distributions is a key issue of understanding the behavior of LFT-D. The essentials points of the methods are described in section 3.2. The prediction of the flow behavior during press compaction is also a very important scientific target to clarify. The very basic portion of the theory is described in Section 4.1. On the other hand, the flow prediction capability of CAE software has been very much improved and some important information, such as local fiber orientations, flow time history, and pressure in molds, can now be predicted, as explained in Section 4.2.

The elastic modulus and strength properties are described in Chapter 5 and the viscoelastic properties are explained in Chapter 6. Owing to information control by project members, the exact values of elastic moduli and strengths cannot be disclosed; rather, relative values are exhibited. The key issue of the elastic moduli is its dependency on local fiber orientations and typical experimental results are indicated.

The joining technology of LFT-D components is one of the key elements of these developments, and an ultrasonic fusion bonding technique was chosen as the primary method. Its concept and typical bonding results with different surface provisions are introduced in Section 7.1. The mechanical properties of bonded C-LFT-D plates are indicated in Section 7.2.

The project outline and its typical results conducted at the University of Tokyo are also introduced in Chapter 8, where the emphasis is placed on CFRTP development as well as its application to automotive structures. The typical material is an assemblage of randomly oriented small rectangle tips of very thin unidirectional thermoplastic prepreg (UT-CTT). Some remarkable essences of their recent papers are explained.

One of very important recent results related to CF composites that has not been presented in this article is a success of the development of the “Innovative Carbon Fiber” conducted in the University of Tokyo group led by Professor Kazuo Kageyama, funded by METI of the Japanese Government. The key point of this success is a development of certain types of CF of very similar mechanical properties to the existing standard class of CF (e.g., T 300) with the possibility of significant production cost reduction. The fundamental technical issue is an omission of the pre-oxidation process of raw polyacrylonitrile (PAN) fiber, sometimes referred to as a “flame-proofing process,” where a large amount of heating energy is consumed. Because of this revolutionary omission of the oxidation process, this new fiber could be produced at quite a low cost in the future, hopefully a half of the existing typical PAN-based carbon fibers costs. If such a fiber is commercially available and its low cost is truly realized, we will be able to see a different world where carbon composites are applied everywhere. For this accomplishment, another review paper might be provided in the future.

CFRTP application activities to automotive structures conducted in Japan, at NCC and the University of Tokyo, are introduced in detail in this article. The authors would be very pleased for this article to be a stimulating trigger of the understanding of Japan's trends of automotive composites and of sincere discussions between worldwide automotive composite engineers.

(403,000 elements, 849,000 fibers).

## Acknowledgements

The authors acknowledge the support from the future-pioneering program commissioned by the gs2:New Energy and Industrial Technology Development Organization (NEDO) for the present development program.

## References

- [1] Takashi Ishikawa, Overview of CFRP (carbon fiber reinforced plastics) application to future automobiles, *J. Soc. Automot. Eng. Jpn.* 68 (2014) 4–11 (in Japanese).
- [2] Website of Toyota Motor Co. LTD, [http://toyota.jp/technology/fuel\\_cell/hybrid/](http://toyota.jp/technology/fuel_cell/hybrid/).
- [3] K. Rohan, T. J. McDonough, V. Ugrestic, E. Potyla, F. Henning, Mechanical study of direct long fiber thermoplastic carbon/polyamid 6 and its relation to processing parameters, Proceedings 14<sup>th</sup> Annual SPE Automotive Composites Conference & Exhibition, 1 June 2015.
- [4] Y. Wan, T. Ohori, J. Takahashi, Mechanical properties and modelling discontinuous carbon fiber thermoplastic, Proceedings of 20th International Conference on Composite Materials, Copenhagen, 19th–24th, July 2015.
- [5] H. Fukuda, T.W. Chou, A probabilistic theory of the strength of short-fibre composites with variable fibre length and orientation, *J. Mater. Sci.* 17 (1982) 1003–1011, <https://doi.org/10.1007/BF00543519>.
- [6] S.Y. Fu, B. Lauke, Effects of fiber length and fiber orientation distributions on the tensile strength of short-fiber-reinforced polymers, *Compos. Sci. Technol.* 56 (1996) 1179–1190, [https://doi.org/10.1016/S0266-3538\(96\)00072-3](https://doi.org/10.1016/S0266-3538(96)00072-3).
- [7] L. Czarnecki, J.L. White, Shear flow rheological properties, fiber damage, and mastication characteristics of aramid-, glass-, and cellulose-fiber-reinforced polystyrene melts, *J. Appl. Polym. Sci.* 25 (1980) 1217–1244, <https://doi.org/10.1002/app.1980.070250623>.
- [8] R. von Turkovich, L. Erwin, Fiber fracture in reinforced thermoplastic processing, *Polym. Eng. Sci.* 23 (1983) 743–749, <https://doi.org/10.1002/pen.760231309>.
- [9] B. Fisa, Mechanical degradation of glass fibers during compounding with polypropylene, *Polym. Compos* 6 (1985) 232–241, <https://doi.org/10.1002/pc.750060408>.

- [10] V.B. Gupta, R.K. Mittal, P.K. Sharma, G. Mennig, J. Wolters, Some studies on glass fiber-reinforced polypropylene. Part I: reduction in fiber length during processing, *Polym. Compos* 10 (1989) 8–15, <https://doi.org/10.1002/pc.750100103>.
- [11] W. Weibull, A statistical distribution function of wide applicability, *J. Appl. Mech.* 18 (1951) 293–297 doi:citeulike-article-id:8491543.
- [12] L.H. Tung, Fractionation of polyethylene, *J. Polym. Sci.* 20 (1956) 495–506, <https://doi.org/10.1002/pol.1956.120209609>.
- [13] S.Y. Fu, C.Y. Yue, X. Hu, Y.W. Mai, Characterization of fiber length distribution of short-fiber reinforced thermoplastics, *J. Mater. Sci. Lett.* 20 (2001) 31–33, <https://doi.org/10.1023/A:1006750328386>.
- [14] S.-Y. Fu, Y.-W. Mai, E.C.-Y. Ching, R.K. Li, Correction of the measurement of fiber length of short fiber reinforced thermoplastics, *Compos. Part A Appl. Sci. Manuf.* 33 (2002) 1549–1555, [https://doi.org/10.1016/S1359-835X\(02\)00114-8](https://doi.org/10.1016/S1359-835X(02)00114-8).
- [15] A.D.S. Jayatilaka, K. Trustrum, Statistical approach to brittle fracture, *J. Mater. Sci.* 12 (1977) 1426–1430, <https://doi.org/10.1007/BF00540858>.
- [16] Y. Masubuchi, M. Terada, A. Yamanaka, T. Yamamoto, T. Ishikawa, Distribution function of fiber length in thermoplastic composites, *Compos. Sci. Technol.* 134 (2016) 43–48, <https://doi.org/10.1016/j.compscitech.2016.08.007>.
- [17] C. Tzoumanekas, D.N. Theodorou, Topological analysis of linear polymer melts: a statistical approach, *Macromolecules* 39 (2006) 4592–4604, <https://doi.org/10.1021/ma0607057>.
- [18] F. Ularych, M. Sova, J. Vokrouhlec, B. Turčić, Empirical relations of the mechanical properties of polyamide 6 reinforced with short glass fibers, *Polym. Compos* 14 (1993) 229–237, <https://doi.org/10.1002/pc.750140308>.
- [19] M.J. Carling, J.G. Williams, Fiber length distribution effects on the fracture of short-fiber composites, *Polym. Compos.* 11 (1990) 307–313.
- [20] N.G. Karsli, A. Aytaç, Tensile and thermomechanical properties of short carbon fiber reinforced polyamide 6 composites, *Compos. Part B* 51 (2013) 270–275.
- [21] K. Rohan, T.J. McDonough, V. Ugresic, E. Potyra, F. Henning, Mechanical study of direct long fiber thermoplastic carbon/polyamide 6 and its relations to processing parameters, *Compos. World* (2015). June 1.
- [22] J.M. Lunt, J.B. Shortall, The effect of extrusion compounding on fibre degradation and strength properties in short glass-fibre-reinforced nylon 6.6, *Plast. Rubber Process* (1979) 108–111.
- [23] J. Müssig, H.G. Schmid, Quality control of fibers along the value added chain by using scanning technique - from fibers to the final product, *Microsc. Microanal.* 10 (2004) 1332–1333.
- [24] M. Terada, A. Yamanaka, Y. Kimoto, D. Shimamoto, Y. Hotta, T. Ishikawa, Evaluation of measurement method for carbon fiber length using general scanner, *Adv. Compos. Mater.*, on submission.
- [25] D.H. Harry, R.G. Parrott, Numerical simulation of injection mold filling, *Polym. Eng. Sci.* 10 (1970) 209–214.
- [26] D. Laroche, K.K. Kabanemi, L. Pecora, R.W. Diraddo, Integrated numerical modeling of the blow molding process, *Polym. Eng. Sci.* 39 (1999) 1223–1233.
- [27] K. Balaji, T.S. Pillay, H. Ning, U.K. Vaidya, Process simulation, design, and manufacturing of a long fiber thermoplastic composite for mass transit application, *Compos. Part A* 39 (2008) 1512–1521.
- [28] P.M. Chaikin, T.C. Lubensky, *Principles of Condensed Matter Physics*, Cambridge University Press, Cambridge, 1995.
- [29] M. Doi, S.F. Edwards, *The Theory of Polymer Dynamics*, Oxford University Press, Oxford, 1986.
- [30] R. Nakano, K. Sakaba, Development of CAE software for injection and BMC/SMC molding including short/long fibers reinforcement, *Proceedings of SMAPE Technical Conf. Seattle 2014*, Seattle, WA, USA, June 2–4, 2014.
- [31] M. Kobayashi, K. Dan, T. Baba, D. Urakami, Compression molding 3D-CAE of discontinuous long fiber reinforced polyamide 6: influence on cavity filling and direct fiber simulations of viscosity fitting methods, *Proceedings of 20th International Conference on Composite Materials (ICCM-20)*, Copenhagen, Denmark, July 19–24, 2015.
- [32] T. Ishizaki, H. Nagano, Measurement of three-dimensional anisotropic thermal diffusivities for carbon fiber reinforced plastics using lock-in thermography, *Int. J. Thermophys.* 36 (2015) 2577–2589.
- [33] R. Fujita, H. Nagano, Novel fiber orientation evaluation method for CFRP/CFRTP based on measurement of anisotropic in-plane thermal diffusivity distribution, *Compos. Sci. Technol.* 140 (2017) 116–122.
- [34] I.M. Ward, J. Sweeney, *An Introduction to the Mechanical Properties of Solid Polymers*, second ed., John Wiley & Sons, 2004.
- [35] L.W. Morland, E.H. Lee, Stress analysis for linear viscoelastic materials with temperature variation, *Trans. Soc. Rheol.* 4 (1960) 233–263.
- [36] K.-H. Kaku, M. Arai, T. Fukuoka, T. Matsuda, Evaluation of thermo-viscoelastic property of CFRP laminate based on a homogenization theory, *Acta Mech.* 214 (2010) 111–121.
- [37] H. Ito, M. Arai, Y. Matsui, D. Itagaki, Experimental testing and FEM simulation for thermal imprinting of micro/nano glass-optical devices, *J. Non-Crystalline Solids* 362 (2013) 246–254.
- [38] O.S. Narayanaswamy, R. Gardon, Stress and volume relaxation in annealing of flat glass, *J. Am. Ceram. Soc.* 53 (7) (1970) 380–385.
- [39] O.S. Narayanaswamy, A model of structural relaxation in glass, *J. Am. Ceram. Soc.* 54 (10) (1971) 491–498.
- [40] Abaqus, Dassault Systèmes, <https://www.3ds.com/products-services/simulia/products/abaqus/>.
- [41] NSYS, ANSYS Inc, <http://www.ansys.com/>.
- [42] Marc, MSC Software Corp., <http://www.mssoftware.com/product/marc>.
- [43] LS-DYNA, Livermore Software Technology Corp., <http://www.lstc.com/products/ls-dyna>.
- [44] J.D. Ferry, *Viscoelastic Properties of Polymers*, second ed., John Wiley & Sons, 1970, pp. 59–87.
- [45] M. Yasui, M. Arai, H. Ito, T. Ino, M. Takahashi, S. Kaneko, Y. Hirabayashi, R. Maeda, Numerical simulation of glass imprinting for molding temperature prediction, *Jpn. J. Appl. Phys.* 49 (6) (2010), 06GL11-T06GL11-4.
- [46] M. Arai, T. Sumida, M. Shimizu, Effect of residual stress on interlaminar fracture toughness of CFRP laminates, *J. Therm. Stresses* 30 (2007) 1099–1116.
- [47] M. Arai, Y. Kato, T. Kodera, Characterization of the thermo-viscoelastic property of glass and numerical simulation of the press molding of glass lens, *J. Therm. Stresses* 32 (2009) 1235–1255.
- [48] K. Imai, Basic Study of Ultrasonic Welding for Carbon Fiber Reinforced Thermo-plastics (CFRTP), Bachelor Thesis, Aerospace Department, Graduate School of Nagoya University, February 2016 (in Japanese).
- [49] T. Ishikawa, Y. Noguchi, M. Matsushima, Processing technique and high fracture toughness of carbon/thermoplastic composites, *J. Jpn. Soc. Compos. Mater.* 13 (2) (1987) 63–71 (in Japanese).
- [50] J. Takahashi, K. Uzawa, T. Matsuo, M. Yamane, Technological Challenges for Realizing Ultra Lightweight Mass Production Automobile by Using CFRTP, ITHEC 2012, Bremen, Germany, 2012.
- [51] J. Takahashi, Development of innovative CFRTP technologies for mass-produced cars, *JEC Compos. Mag.* 81 (2013) 44–45.
- [52] J. Takahashi, T. Ishikawa, Next Challenge in CFRTP for Mass Production Automotive Application, SAMPE SEICO 14, Paris, France, 2014.
- [53] J. Takahashi, T. Ishikawa, Recent Japanese Activity in CFRTP for Mass Production Automobile, ITHEC 2014, Bremen, Germany, 2014.
- [54] S. Yamashita, I. Ohsawa, T. Matsuo, X. Zhang, J. Takahashi, Evaluation of Young's modulus and out-of-plane shear modulus of carbon fiber reinforced thermoplastics by three point bending test, *J. Jpn. Soc. Compos. Mater* 39 6 (2013) 221–230.
- [55] Y. Wan, J. Takahashi, Tensile and compressive properties of chopped carbon fiber tapes reinforced thermoplastics with different fiber lengths and molding pressures, *Compos. Part A* 87 (2016) 271–281.
- [56] S. Yamashita, K. Hashimoto, H. Suganuma, J. Takahashi, Experimental characterization of the tensile failure mode of ultra-thin chopped carbon fiber tape-reinforced thermoplastics, *J. Reinf. Plast. Compos* 35 18 (2016) 1342–1352.
- [57] H. Suganuma, S. Yamashita, I. Ohsawa, J. Takahashi, Research on the scatter in the evaluation test of tensile modulus of ultra-thin chopped carbon fiber tape reinforced thermoplastics, *J. Jpn. Soc. Compos. Mater* 43 1 (2017) 18–24.
- [58] X. Lyu, J. Takahashi, Y. Wan, I. Ohsawa, Determination of transverse flexural and shear moduli of chopped carbon fiber tape reinforced thermoplastic by vibration, *J. Compos. Mater* (2017), <https://doi.org/10.1177/0021998317707815>.
- [59] Y. Wan, I. Straumit, J. Takahashi, S.V. Lomov, Micro-CT analysis of internal geometry of chopped carbon fiber tapes reinforced thermoplastics, *Compos. Part A* 91 (2016) 211–221.
- [60] Y. Wan, J. Takahashi, Tensile properties and aspect ratio simulation of transversely isotropic discontinuous carbon fiber reinforced thermoplastics, *Compos. Sci. Technol.* 137 (2016) 167–176.
- [61] I. Ohsawa, J. Takahashi, Micro droplet test and evaluation of interfacial shear strength of CF/PP, *Reinf. Plast.* 59 9 (2013) 330–336.
- [62] H. Lee, I. Ohsawa, J. Takahashi, Effect of plasma surface treatment of recycled carbon fiber on carbon fiber-reinforced plastics (CFRP) interfacial properties, *Appl. Surf. Sci.* 328 (2015) 241–246.
- [63] H. Lee, H. Wei, J. Takahashi, The influence of plasma in various atmospheres on the adhesion properties of recycled carbon fiber, *Macromol. Res.* 23 11 (2015) 1026–1033.
- [64] M. Wada, K. Kawai, T. Suzuki, H. Hira, S. Kitaoka, Effect of superheated steam treatment of carbon fiber on interfacial adhesion to epoxy resin, *Compos. Part A* 85 (2016) 156–162.
- [65] H. Wei, H. Lee, W. Nagatsuka, I. Ohsawa, K. Kawabe, T. Murakami, K. Sumitomo, J. Takahashi, Systematic Comparison between Carding and Paper-making Method for Producing Discontinuous Recycled Carbon Fiber Reinforced Thermoplastics, ICCM20, Copenhagen, Denmark, 2015.
- [66] W. Nagatsuka, T. Matsuo, F. Yano, J. Takahashi, Prediction about time-dependent flexural modulus of discontinuous and dispersed carbon fiber mat reinforced thermoplastics, *J. Jpn. Soc. Compos. Mater* 42 1 (2016) 23–33.
- [67] T. Otori, H. Lee, I. Ohsawa, J. Takahashi, Optimal structural design of discontinuous carbon fiber reinforced thermoplastic plates subjected to bending loads, *J. Jpn. Soc. Compos. Mater* 43 2 (2017) 65–73.
- [68] R. Shida, J. Takahashi, Theoretical analysis on CFRTP optimal variable thickness beam subjected to bending load and the influence of out-of-plane shear modulus, *J. Jpn. Soc. Compos. Mater* 43 4 (2017).
- [69] Y. Wan, T. Matsuo, I. Ohsawa, J. Takahashi, Effects of curvature on strength and damage modes of L-shaped carbon fiber reinforced polypropylene, *J. Reinf. Plast. Compos* 33 14 (2014) 1305–1315.
- [70] T. Matsuo, T. Goto, J. Takahashi, Investigation about the fracture behavior and strength in a curved section of CF/PP composite by a thin-curved beam specimen, *Adv. Compos. Mater* 24 3 (2015) 249–268.
- [71] S. Yamashita, I. Ohsawa, T. Matsuo, J. Takahashi, Research on soft skin effect of carbon fiber reinforced polypropylene, *J. Jpn. Soc. Compos. Mater* 39 5 (2013) 176–183.

- [72] S. Yamashita, I. Ohsawa, J. Takahashi, Study on fracture behavior of carbon fiber reinforced thermoplastics under artificial lightning strike by impulse current generator, *J. Jpn. Soc. Compos. Mater* 40 1 (2014) 17–24.
- [73] S. Yamashita, Y. Nakashima, J. Takahashi, K. Kawabe, T. Murakami, Volume resistivity of ultra-thin chopped carbon fiber tape reinforced thermoplastics, *Compos. Part A* 90 (2016) 598–605.
- [74] S. Yamashita, T. Sonehara, J. Takahashi, K. Kawabe, T. Murakami, Effect of thin-ply on damage behavior of continuous and discontinuous carbon fiber reinforced thermoplastics subjected to simulated lightning strike, *Compos. Part A* 95 (2017) 132–140.
- [75] Y. Wan, J. Takahashi, Deconsolidation behavior of carbon fiber reinforced thermoplastics, *J. Reinf. Plast. Compos* 33 17 (2014) 1613–1624.
- [76] T. Hayashi, T. Kobayashi, J. Takahashi, Influence of void content on the flexural fracture behaviour of carbon fiber reinforced polypropylene, *J. Compos. Mater* (2017), <https://doi.org/10.1177/0021998317698215>.
- [77] T. Hayashi, T. Kobayashi, J. Takahashi, Quantification of void fraction of composite materials by soft X-ray transmittance, *J. Jpn. Soc. Compos. Mater* 41 4 (2015) 122–127.
- [78] T. Hayashi, T. Kobayashi, J. Takahashi, Quantification of the void content of composite materials using soft X-ray transmittance, *J. Thermoplast. Compos. Mater* (2016), <https://doi.org/10.1177/0892705716644670>.
- [79] T. Hayashi, T. Kobayashi, J. Takahashi, Soft X-ray attenuation coefficient of composite materials, *J. Jpn. Soc. Compos. Mater* 42 5 (2016) 169–177.